

Probing the structure of cyclic hydrocarbon molecules with X-ray-induced Coulomb explosion imaging [†]

Kurtis D. Borne^{a,b}, Rebecca Boll^c, Thomas M. Baumann^c, Surjendu Bhattacharyya^{a,b}, Martin Centurion^d, Keyu Chen^a, Benjamin Erk^e, Alberto De Fanis^c, Ruaridh Forbes^{b,f}, Markus Ilchen^{c,e,g}, Edwin Kukk^h, Huynh V. S. Lam^a, Xiang Li^b, Lingyu Maⁱ, Tommaso Mazza^c, Michael Meyer^c, Terence Mullins^{c,e,l}, J. Pedro F. Nunes^d, Asami Odateⁱ, Shashank Pathak^a, Daniel Rivas^c, Philipp Schmidt^c, Florian Trinter^j, Sergey Usenko^c, Anbu S. Venkatachalam^a, Enliang Wang^{a,k}, Peter M. Weberⁱ, Till Jahnke^c, Artem Rudenko^a, and Daniel Rolles^{a,*}

Received Date

Accepted Date

DOI: 00.0000/xxxxxxxxxx

Coulomb explosion imaging (CEI) is a powerful experimental technique that maps a molecule's geometric structure onto the momenta of ionic molecular fragments produced by rapid multiple ionization. Here, we apply CEI induced by pulses from an X-ray free-electron laser in order to image and distinguish complex hydrocarbon isomers with the chemical formula C₇H₈: toluene, cycloheptatriene, and 1,6-heptadiyne. The measured fragment-ion momentum distributions show discernible differences between the three isomers and provide signatures of specific carbon and hydrogen sites in the molecule. In contrast to previous work, we demonstrate that distinct 'marker atoms' are not strictly required for constructing a meaningful molecular frame of reference for the interpretation of the momentum-space data. Our work paves the way for tracking the ultrafast motion of nuclei during isomerization reactions in pure hydrocarbons.

1 Introduction

Coulomb explosion imaging (CEI) is an experimental technique that encodes information about a molecule's nuclear geometry in the momenta of ionic fragments produced when the molecule breaks apart after being multiply ionized. The key to CEI is *rapid* removal of multiple electrons, thus populating a highly charged cationic state, on which the molecule fragments – ideally completely into individual atomic ions.^{1–3} If enough electrons are removed and the molecule does not undergo significant structural rearrangement during the ionization process, the measured asymptotic momenta of the fragment ions provide information about the molecular geometry prior to ionization. This infor-

mation can be extracted, e.g., by comparing the measured momenta to predictions of a Coulomb explosion model, thus providing a link between the real-space molecular geometry and the observed fragment-ion momentum distribution.^{4–9} Various methods can be employed for the ionization step, including colliding molecular ions with thin foils^{1,10,11}, ion-neutral cross-beam collisions^{12–15}, and different ionizing radiation sources such as femtosecond lasers^{2,4,6,16–21}, synchrotrons^{22,23}, or free-electron lasers^{3,5,7,24,25}. Similarly, the generated fragment ions can either be imaged in a non-coincident manner^{17,26–31} or by performing coincidence measurements in order to extract correlated information on a single-molecule level^{1–8,11–15,20–25,32,33}.

Several studies used CEI specifically to differentiate molecular isomers. For example, CEI induced by soft X-ray synchrotron radiation was used to distinguish geometric isomers and conformers of halogenated hydrocarbons^{22,23,34}. However, a single photoabsorption in the soft X-ray range generates only a few charges per molecule – typically two to three, unless heavy atoms are present that enhance ionization. For polyatomic molecules in which the number of atoms exceeds the number of charges generated, single photoabsorption therefore does not lead to a complete breakup into individual atomic ions. In contrast, using intense soft X-ray pulses from an X-ray free-electron laser (XFEL) can result in very high charge states through multiple inner-shell ionizations and Auger decay cascades, thus triggering a complete breakup into atomic ions even for molecules with ten or more atoms. This has enabled complete CEI of CH₃I⁵ and of several heterocyclic molecules containing strong absorption sites such as iodine and sulfur.^{3,7,24} Complete Coulomb explosion can also be induced by intense near-infrared femtosecond laser pulses,

^a J. R. Macdonald Laboratory, Department of Physics, Kansas State University, Manhattan, KS, USA

^b Linac Coherent Light Source, SLAC National Accelerator Laboratory, Menlo Park, CA, USA

^c European XFEL, Schenefeld, Germany

^d Department of Physics and Astronomy, University of Nebraska–Lincoln, Lincoln, NE, USA

^e Deutsches Elektronen-Synchrotron DESY, Hamburg, Germany

^f Department of Chemistry, University of California, Davis, CA, USA

^g Department of Physics, University of Hamburg, Hamburg, Germany

^h Department of Physics and Astronomy, University of Turku, Turku, Finland

ⁱ Department of Chemistry, Brown University, Providence, RI, USA

^j Molecular Physics, Fritz-Haber-Institut der Max-Planck-Gesellschaft, Berlin, Germany

^k Hefei National Research Center for Physical Sciences at the Microscale and Department of Modern Physics, University of Science and Technology of China, Hefei, China

^l The Hamburg Centre for Ultrafast Imaging, Universität Hamburg, Hamburg, Germany

* email: rolles@ksu.edu

† Supplementary Information available: [details of any supplementary information available should be included here]. See DOI: 10.1039/cXCP00000x/

which was used, e.g., to image the structure of molecules such as a biphenyl derivative^{26,35}, bromochlorofluoromethane², tribromomethane⁴, furan³⁶, and several other organic molecules containing unique marker atoms^{6,32}.

When used in a pump-probe scheme with femtosecond near-infrared or X-ray pulses, CEI can also be used to visualize structural changes in gas-phase molecules.^{8,16,18,20,21,24-26,35,36} Compared to other ultrafast gas-phase molecular imaging techniques such as ultrafast electron diffraction or hard X-ray scattering³⁷⁻³⁹, CEI has a few notable differences that can be advantageous for certain types of studies. For example, obtaining structural information on light atoms such as hydrogen is challenging in electron diffraction and X-ray scattering due to their small atomic scattering form factors as compared to heavier atoms with higher nuclear charge⁴⁰⁻⁴², making it extremely difficult to image the positions of hydrogen atoms in larger hydrocarbons. Coulomb explosion imaging, on the other hand, has the same sensitivity to light and heavy species and is inherently sensitive to the full 3D structure, including all bond angles, not just atomic pair distances. Nevertheless, the direct extraction of position-space geometries from measured momentum-space data is far from trivial. So far, it has been performed routinely only for small molecules consisting of 2-3 atoms and represents a significant challenge for larger molecules.^{5,43} In addition, for larger molecules, CEI has been successfully applied in the past mainly to systems with unique 'marker' atoms. These markers facilitate the definition of a molecular frame of reference for the interpretation of the measured results^{7,20,24}. An application of CEI to pure hydrocarbons with more than two carbon atoms has been little explored to date.

In the present work, we study Coulomb explosion of three different isomers with the chemical formula C₇H₈: toluene, cycloheptatriene, and 1,6-heptadiyne, shown in Fig. 1)A-C. Toluene consists of a methyl group attached to a phenyl ring; cycloheptatriene is a non-planar seven-membered ring; and 1,6-heptadiyne consists of a seven-membered carbon chain that has several conformers, as discussed in more detail in section 3.5. These molecules have several interesting and challenging features with regards to CEI: First, there is no preferential absorption site within these molecules. Second, they lack unique 'marker atoms' that could serve to define the molecular frame. Third, their different geometries provide an opportunity to investigate if CEI can distinguish different isomers that could be formed, e.g., as reaction products of a ring-opening or ring-reconfiguration reaction of pure hydrocarbons. In the present work, we address the impact of these aspects for momentum imaging.

2 Methods

2.1 Experiment

The experiment was performed at the Small Quantum Systems (SQS) scientific instrument of the European XFEL⁴⁴ using the cold target recoil ion momentum spectroscopy (COLTRIMS) reaction microscope (REMI) endstation. This experimental setup has been described in previous publications^{3,5,45-47} and is only summarized here. The liquid samples were contained in a stainless-steel sample reservoir at room temperature, and their vapor was

delivered into the vacuum chamber as a molecular beam expanded through a 200 μm flat nozzle without the use of a carrier gas. The molecular beam was collimated by passing it through four differential pumping stages, each separated by a molecular beam skimmer or aperture.

The ion spectrometer used in this experiment was similar to that used in Refs.^{3,33}. It consisted of an acceleration region with a length of 50 mm, followed by a drift region with a length of 130 mm with no mesh in between these two regions. The electric field at the target region was set to approximately 325 V/cm. The ions were detected on a 120-mm diameter MCP with an applied voltage of -2.5 kV across the chevron stack, followed by a hexagonal delay-line anode assembly held at ground. The ions originating from each X-ray pulse were measured in coincidence. The analog detector signals were recorded using fast (1.8 GS/s) analog-to-digital converters. An average of 4 ion hits per X-ray pulse were recorded, of which an average of 2 ion hits per pulse originated from the molecular beam.

The European XFEL operated with self-amplified spontaneous emission (SASE) at a base repetition rate of 10 Hz, providing bursts of electron bunches with an intra-train repetition rate of 1.1 MHz. To acquire the data shown here, every sixth electron pulse was used to generate 1.5-keV X-ray pulses, yielding an effective rate of 600 soft X-ray pulses per second for the experiment. The average single-shot pulse energy was up to 4 mJ, as measured by a gas monitor detector upstream of the beamline optics.⁴⁸ Given an estimated beamline transmission of 80%,⁴⁹ this resulted in an average pulse energy of up to 3.2 mJ at the interaction point. The X-ray pulses were focused using a pair of Kirkpatrick-Baez mirrors, and the focus spot size was estimated to be 1.4 μm diameter FWHM. The estimated upper limit of the X-ray pulse duration based on the electron bunch charge of 250 pC in the accelerator is 25 fs (FWHM). However, dedicated tuning of the undulator settings with feedback from the SASE3 grating spectrometer before the data taking suggests significantly shorter pulse durations based on spectral analysis for the present experiment.

2.2 Coulomb explosion simulations

Numerical simulations of the Coulomb explosion process were performed by solving $3N$ coupled differential equations for classical point particles of mass m_i and charge q_i , located at positions \vec{r}_i , undergoing mutual Coulomb repulsion. The simulations assumed an instantaneous charge-up to the final charge state, and the initial coordinates of the ions were defined by the molecular geometry as described below. The system of equations was defined by Newton's second law under the Coulombic force:

$$m_i \frac{d^2}{dt^2} \vec{r}_i(t) - \sum_{j=1}^N q_i q_j \frac{\vec{r}_i(t) - \vec{r}_j(t)}{(\vec{r}_i(t) - \vec{r}_j(t))^{3/2}} = 0 \quad (1)$$

To model the experimental results presented in the main text, all carbon atoms were doubly charged ($q = 2$), and all hydrogen atoms were singly charged ($q = 1$) in order to match the coincidence channel that was selected in the data analysis. To simulate the influence of the inherent uncertainty of the atomic

positions due to zero-point quantum fluctuations³³ on the momentum imaging, several thousand geometries with initial positions reflecting the zero-point energy vibrational distributions ('Wigner distribution') were generated. First, the neutral electronic ground-state geometry of each molecule was determined using the universal force field molecular optimization method with the Babel extension in Avogadro-2^{50,51}. This geometry was then used in the Newton-X software⁵² to sample 10,000 geometries of the distribution in the ground state at 0 K. While several earlier CEI studies have shown that sampling the Wigner distribution typically leads to a significantly narrower spread of the simulated ion momenta than what is observed experimentally^{4,6,7,32}, the narrower features in the simulated momentum images make it easier to identify the contributions from different molecular reference frames, and we therefore chose not to add additional broadening to the simulations.

3 Results and Discussion

3.1 Molecular-frame momentum-space results

In this section, we first discuss the experimental results and their comparison for the three isomers in general terms, followed by a discussion of the simulation results for the three isomers. In sections 3.3 through 3.5, we revisit the results for each isomer in detail and discuss how the Coulomb explosion images can be improved by using additional angular correlations to better define a molecular reference frame. Finally, while the aforementioned sections focus on carbon ions, section 3.6 presents experimental and simulated results for the emitted H⁺ ions.

Figure 1 panels D) through F) show the experimental recoil-frame ion momentum distributions of doubly charged carbon ions obtained by detecting three C²⁺ ions in coincidence after multi-photon X-ray ionization of D) toluene, E) cycloheptatriene, and F) 1,6-heptadiyne in the form of *Newton plots*. Newton plots display the momentum distribution of each ion within a molecular *recoil frame* defined by two selected ions. In this coordinate frame, one of the ion momenta (\vec{p}_i) defines the x-axis. Together with the momentum vector of a second ion (\vec{p}_j), it spans the *recoil plane* incorporating the x-axis and the y-axis. The z-axis is defined as the normal to the recoil plane yielding a right-handed coordinate frame. The momenta of other measured fragments are transformed into this coordinate frame and plotted. For the plots shown here, the two reference ions as well as the third ion plotted in the figures were all selected to be C²⁺, and the two reference ions were randomly chosen from these three ions. We chose the C²⁺-C²⁺-C²⁺ three-particle coincidence channel for the analysis because it is a relatively strong channel with sufficient statistics and because the charge of +2 on each ion implies that the molecule was ionized to a relatively high total charge state. The latter increases the likelihood that each atom in the molecule carried at least one charge during the explosion, which improves the quality of the Coulomb explosion images and facilitates comparison with our relatively simple model assuming purely Coulombic repulsion of classical point charges. Similar Newton plots for toluene for other strong three-particle coincidence channels containing one or several C⁺ fragments are shown in Fig. 6 in the Supplementary Material.

As discussed above, in our previous CEI studies^{2,3,6,7,24}, the molecules under investigation consisted of at least two unique atomic constituents, allowing us to define the recoil frame for each molecule in a straightforward and intuitive way. The pure hydrocarbons studied here do not have such uniquely distinguishable atoms, which leads to an ambiguity in the assignment of the molecular frame based on the measured C²⁺ ion momenta. For example, the molecule sketched in Fig. 1A) is oriented with the methyl group pointing along the positive p_x -axis. However, as long as the reference ions are randomly chosen from the detected C²⁺ ions and no other metrics are used to identify the emission site of a given ion, this specific orientation is only realized in a subset of events in which the carbon atom of the methyl group was (by chance) selected as the ion with momentum \vec{p}_i . In other cases, any of the other carbon ions maybe have been used to define the molecular-frame x-axis. The experimental Newton plots in Figs. 1D-F) are thus comprised of 42 different recoil frames (corresponding to the number of permutations of 2 items selected from a set of 7). We detail in sections 3.3 through 3.5 how this problem can be circumvented to some extent.

Despite this summing over several different recoil frames, distinct differences between the three isomers can already be identified in Figs. 1D-F). The ion momenta of toluene (Fig. 1D) exhibit the most structured Newton plot with six distinct peaks in the (p_x/p_y)-plane. In the (p_y/p_z)-plane, a low-momentum peak is surrounded by a distinct ring of higher momenta, but the distribution has a maximum at $p_z = 0$. The cycloheptatriene momentum distribution (Fig. 1E) does not have distinct peaks in the (p_x/p_y)-plane. However, it also shows a high-momentum ring in the (p_x/p_z)-plane, but without a clear maximum at $p_z = 0$ and without the low-momentum peak. Finally, the 1,6-heptadiyne Newton plot (Fig. 1F) shows a reminiscence of the ring in the (p_y/p_z)-plane, but significantly broadened compared to the other two molecules. Otherwise, the Newton plot shows a rather structureless distribution in all three planes.

3.2 Simulation results

In order to help with interpreting the experimental results, classical Coulomb explosion simulations are performed that can be used to assign the features observed in the experimental data. In the simulations, the momentum of each fragment ion under the influence of purely Coulombic interactions with the other ions is calculated in the center-of-mass frame, as described in section 2.2. The results are shown in Fig. 1, panels G-I). The momenta for each pair of two ions are used to construct the recoil frame, and the corresponding Newton plots for each possible recoil frame (see Fig. 2 for examples of some of the recoil frames) are combined to yield a simulated plot that can be directly compared to the experimental plots.

In the simulation, it is possible to specify which ions from certain atomic sites in the molecule are used as reference ions for the recoil frame. As expected, the features in the Newton plots vary significantly depending on the choice of reference ions. This observation is exemplified using toluene in Fig. 2, where several simulated Newton plots with reference ions from different car-

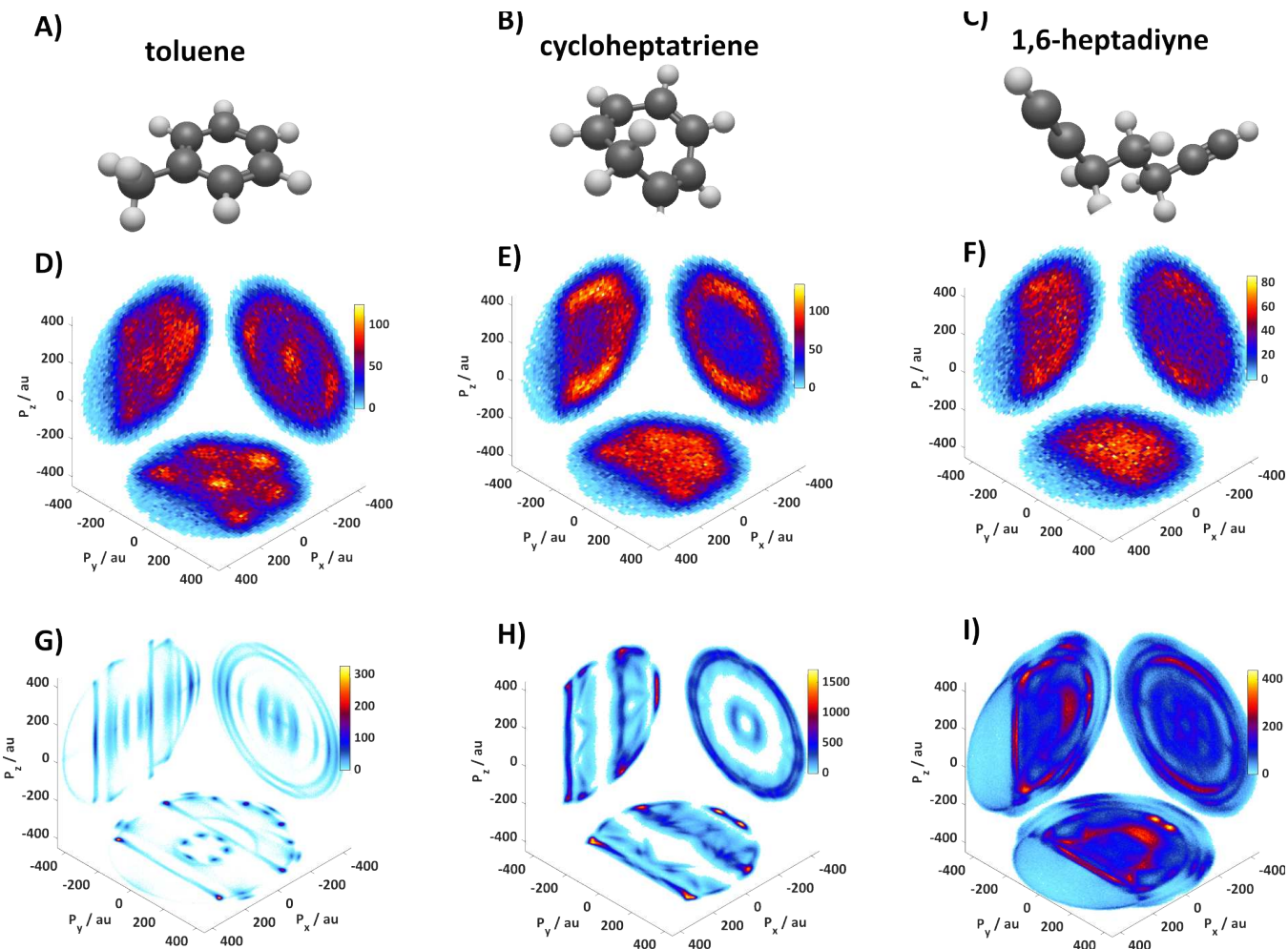


Fig. 1 Molecular geometries and Newton plots: A) toluene, B) cycloheptatriene, C) 1,6-heptadiyne. D)-F) Experimental Coulomb explosion Newton plots showing the momentum distribution (in atomic units, a.u.) of three C^{2+} ions detected in coincidence. The molecular frame is defined by orienting the emission direction of one C^{2+} ion, which is randomly chosen among the three detected C^{2+} ions, along the positive p_x -direction and the emission direction of another C^{2+} ion, also randomly chosen from the three ions detected in coincidence, in the upper half of the (p_x/p_y) -plane. G)-I) Simulated Newton plots for C^{2+} , built by adding the simulated momentum distributions in all the recoil frames obtained from all possible combinations of two C^{2+} ions, as explained in sections 2.2 and 3.2. In the simulations, a charge of +2 is placed on each carbon atom and +1 on each hydrogen atom.

bon sites in the molecule are shown. The momentum for each fragment ion is represented as color-coordinated points (allowing identification of the atomic site in the molecule), and the overall recoil-frame momentum distribution is projected onto the three planes (x,y), (x,z), and (y,z), in analogy to the representation in Fig. 1. Some of these Newton plots are very reminiscent of the six-membered ring geometry of toluene, e.g., Fig. 2 panels A) and B), while in others, shown in Fig. 2 panels C) and D), obvious similarities are lost, as features become very diffuse in all three planes. The reason for this behavior can be seen, for example, in panel C), where the two ions defining the recoil frame are emitted close to back-to-back, thus not providing a well-defined recoil plane. We therefore conclude that it would be beneficial for the determination of the molecular structure to try to select, as much as possible, which recoil frames contribute to the Newton plots of the experimental data such that unsuitable combination can be excluded, as opposed to including all combinations of reference pairs. Thus, in the following, we investigate ways to identify

the molecular site from which specific ions originate in the experiment. Since the specifics depend on the particular molecular structure, we discuss each isomer separately.

3.3 Toluene

Toluene is a planar molecule consisting of a methyl group attached to a six-membered phenyl ring. Some features in the Newton plot of Coulomb-exploded toluene reflect its cyclic geometry, as shown in Fig. 1 D and G. In the measured data, there are five distinct peaks in the (p_x/p_y) -plane, which are approximately equidistant from the origin, and one peak lying near the origin of the (p_x/p_y) -plane. The five outer peaks correspond to the high-energy emission of the carbons on the phenyl ring (C3-C7, as labeled in Fig. 2) and the substituted methyl carbon (C1). The carbon to which the methyl group is attached (carbon C2) corresponds to the low-energy feature near the center of the (p_x/p_y) -plane because emission of carbon C2 is impeded due to opposing Coulomb repulsion from its neighboring ions at the methyl site

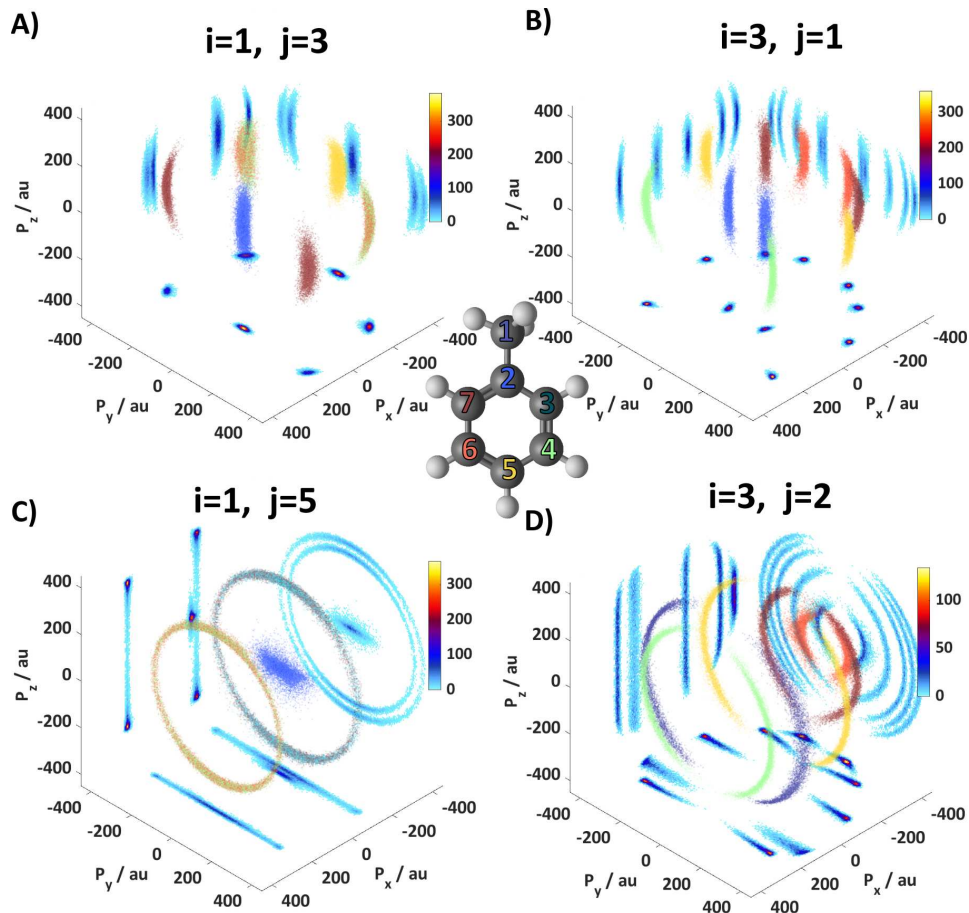


Fig. 2 Simulated three-dimensional Newton plots of toluene, plotted for different combinations of reference ions, corresponding to different carbon sites in the molecule. Carbon i denotes the ion momentum that defines the x -axis, while carbon j is that which lies within the (x,y) -plane, with the numbering of the carbon atoms and the color coding of the scatter plot symbols referring to the ball-and-stick model of the molecule shown at the center of the figure. The momenta of the two reference ions are not shown in this representation, and projections of the momentum distributions on the three Cartesian planes are shown in light blue to aid with the three-dimensional visualization.

and the rest of the carbon ring (also known as 'obstructed fragmentation'⁵³). A similar behavior was observed in the Coulomb explosion of other cyclic molecules with a heavy substituent^{3,7}.

Comparing the simulation results in Fig. 1G with the measured data, we find similarities but also distinct differences. First, the fact that the absolute momenta of the carbon atoms in the simulation (which are centered around $|\mathbf{p}| \approx 400$ a.u.) are approximately twice the value of the experiment, where the outer peaks are centered around $|\mathbf{p}| \approx 200$ a.u., clearly indicates that the approximations made in the simulations are not suitable for accurately describing the absolute momentum magnitudes. Most notably, these assumptions are the instantaneous charge-up to the final charge state, the assumption of purely Coulombic potential energy surfaces of the highly charged ion, and also the assumption of a charge of 2+ for *each* carbon and 1+ for *each* hydrogen atom. In the experiment, the charges on the undetected ions are unknown and thus lead to a significant variation of the recoil momentum. However, as also observed in earlier work^{3,6,7,24}, despite overestimating the momentum magnitudes, such simulations typically reproduce the relative emission directions of the molecular fragments very well, albeit significantly underestimating

the angular spread of each of the peaks. We can therefore use the simulation results to guide our attempts of better defining the recoil frame, as described in section 3.3.1. In the simulated data, the aforementioned five outer peaks as well as the inner peak in the (p_x/p_y) -plane exhibit a clear sub-structure. This sub-structure in the simulated Newton plot results from the inclusion of all possible recoil frame combinations: The simulations in Fig. 2 show that Newton plots, where the carbon from the methyl group (C1) and a carbon other than C2 or C5 are chosen as references, provide an intuitive picture of the molecular geometry in the (p_x/p_y) -plane. However, when a different combination of reference ions is chosen, e.g., in Fig. 2B, all the peaks are slightly shifted, as can also be seen clearly in Fig. 7 in the Supplementary Material, which shows the Newton plots for all possible combinations of reference ions. These shifts are an additional reason why the experimental distributions are so broad, since in the experimental Newton plots, we integrated over all possible combinations of reference ions.

In addition, if the reference ions are emitted anti-parallel, i.e., back-to-back, the reference ion j will have no perpendicular component to reference ion i , and the (p_x/p_y) -plane in the recoil

frame is thus ill-defined. This causes several features in the Newton plot to be dispersed along one of the axes in the projections, as shown in Fig. 2C. Similarly, if the ion corresponding to the obstructed fragment (carbon C2) is included as one of the reference ions, the (p_x/p_y) -plane is also ill-defined, as this ion has a momentum close to $|\vec{p}| = 0$ a.u. and thus an almost arbitrary emission direction compared to the other ions. In the recoil frame, this leads to strongly dispersed momentum distributions, especially outside the recoil plane, as shown in Fig. 2D.

3.3.1 Identification of specific carbon ions via angular correlation metrics

The preceding subsection demonstrated the need for means to further identify experimentally which of the different carbon ions of the toluene molecule were detected in each triple-coincidence event in order to disentangle the different recoil frames that contribute to Fig. 1D). One advantage of momentum-resolved multi-particle coincidence measurements is that there are additional correlations that encode information on the molecular fragmentation, which can be used in particular for identifying suitable reference ions. As we show in the following, events can be selected in which the momenta of the measured carbon ions meet certain criteria in their correlations that correspond to a specific carbon site (or subset of sites) inside the molecule. Such a selection reduces the number of recoil frames that contribute to a Newton plot, thus providing a cleaner and more intuitive Coulomb explosion pattern. For example, removing ions with low kinetic energy from the set of reference ions reduces the likelihood that the recoil plane is ill-defined because the reference ions do not include the carbon C2, which is undergoing obstructed breakup. Moreover, the relative emission angle between two carbon ions provides information on the relative positions of these carbons in the molecule.

A procedure for making use of some of this information is exemplified in Fig. 3. Panel A) shows the distribution of relative emission angles between any two selected ions that are used as the reference ions i and j as obtained from both the experimental (blue) and simulated (red) data. As noted before, the features observed in the experiment are much broader than those obtained in the simulation but occur in the same angular ranges. Using the simulation data, we computed the average value $\langle \cos(\theta_{i,j}) \rangle$ of these relative emission angles for different pairs of ions and summarized the resulting values in the matrix shown in Fig. 3B. The values are color-coded for illustrative purposes. This matrix reveals that the peak at $\cos(\theta_{i,j}) = -1$ stems from pairs of carbon atoms located on opposite sides of the phenyl ring, while the smaller peak near $\cos(\theta_{i,j}) = +1$ is due to the nearly parallel emission of the methyl carbon (C1) and carbon C2. The peaks near $\cos(\theta_{i,j}) \approx +0.4$ and ≈ -0.5 correspond to neighboring and alternating carbons within the phenyl ring, respectively.

Using the assignment obtained from the simulation, we can identify the contribution of ion pairs to the broad peaks in the measured angular distribution. Exploiting this information, it is possible to improve the clarity of the measured Newton plots by filtering on the relative emission angle between the reference ions. Panel C) shows once again the Newton plot with-

out filtering, thus containing all reference combinations. Note that we removed a random subset of the data to obtain a similar amount of statistics as in panels D) and E) and thus facilitate a direct comparison. The Newton plots shown in panels D) and E) contain only those events in which the reference ions are emitted at relative angles $\cos(\theta_{i,j}) \in \{-0.805, -0.155\}$ and $\cos(\theta_{i,j}) \in \{0.025, 0.675\}$, respectively. Additionally, these reference ions are selected to have a kinetic energy larger than 1 a.u., to avoid including the obstructed carbon C2 as a reference ion, which degrades the clarity of the Newton plots as mentioned above (see Figs. 2C and 2D). With this filtering, the Newton plots become more structured as the number of contributing recoil frames in the Newton plot is greatly reduced, from 42 to no more than sixteen possible reference combinations, and the reference ions are primarily pairs of alternating or neighboring carbons (in panels D) and E), respectively). This interpretation is confirmed by the notable reduced intensity of the peak on the positive and negative side of the p_x -axis, respectively. It would be in these empty spaces where the reference ion j would appear, but this reference ion is not plotted here for the sake of demonstrating the efficiency of the filtering method.

3.4 Cycloheptatriene

Cycloheptatriene (CHT) is a seven-membered cyclic hydrocarbon. It has a non-planar chair conformation in its ground-state geometry. Because of the non-planarity, we expect a larger magnitude of the out-of-plane momenta than in the case of the toluene molecule. Indeed, this expectation is confirmed when inspecting the measured and simulated results of Coulomb-exploded CHT, which are shown in panels E) and H) of Fig. 1. The momentum distributions of the recoiling ions have strong contributions outside of the recoil plane defined by any combination of two reference ions and do not show a maximum at $p_z = 0$. Furthermore, unlike the case of the planar toluene molecule, where the Newton plot had some resemblance to the molecular geometry, both the experimental and simulated Newton plots for CHT are much less intuitive. As for toluene, selecting reference ions based on their relative emission angles can reduce the number of contributing recoil frames, enabling easier mapping of features in the Newton plots to sites in the molecule. The distribution of relative emission angles is shown in Fig. 4A) for both the simulated and experimental data. The large peak near $\cos(\theta_{i,j}) = -1$ is due to anti-parallel emission of carbon atoms located on opposite sides of the molecular ring. Emission of ions from neighboring carbon sites (e.g., $i = 2$ and $j = 3$) corresponds to peaks near $\cos(\theta_{i,j}) \approx 0.5$, while ions from alternating carbon sites (e.g., $i = 2$ and $j = 4$) make up the peaks near $\cos(\theta_{i,j}) \approx -0.6$. These features observed in the relative emission angle distribution for this seven-membered carbon ring are analogous to those belonging to the phenyl ring in toluene. We provide a matrix showing the average values of $\langle \cos(\theta_{i,j}) \rangle$ for different pairs of ions in panel B) of Fig. 4 just as in the previous subsection on toluene.

Panels C) and E) of Fig. 4 show the simulated and experimental Newton plots after gating on the aforementioned relative angle region associated with alternating carbons in the ring. The

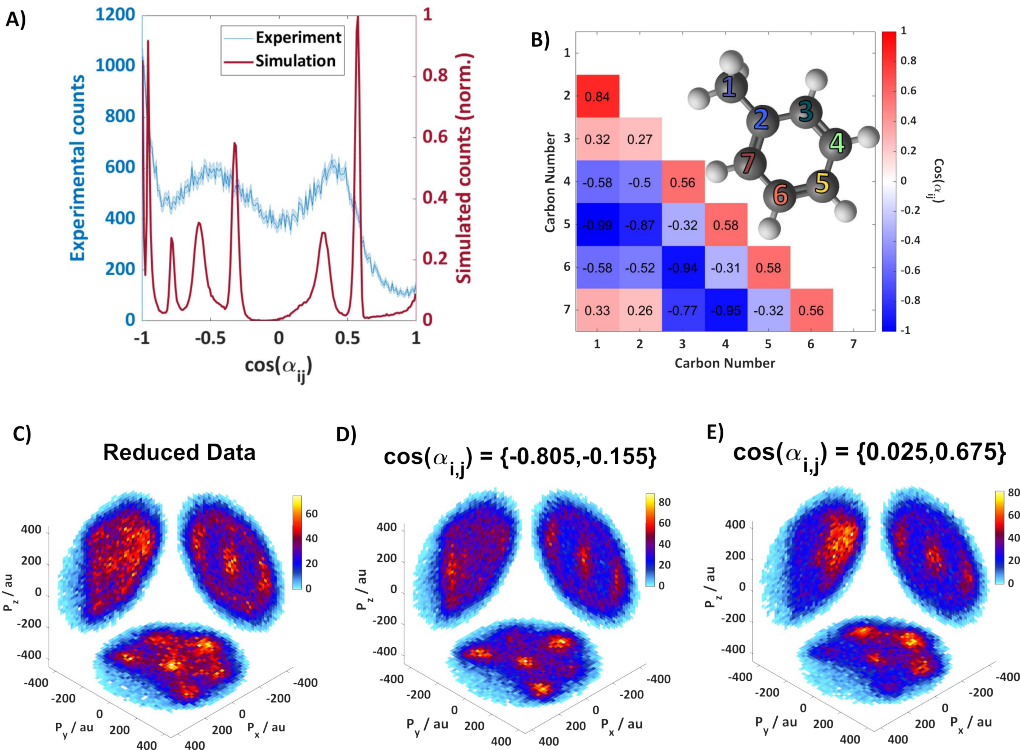


Fig. 3 Data filtering on angular correlations of the reference ions employed for defining the recoil frame of the toluene Newton plots. A) Simulated (red) and experimental (blue) distribution of the relative emission angle of the two ions i and j used to define the recoil frame. B) Matrix showing the average $\langle \cos(\theta_{i,j}) \rangle$ in the simulated datasets for different combinations of carbon ions. This matrix acts as a guide for which gating region corresponds to which reference ions defining the Newton plot. Darker blue colors correspond to $\langle \cos(\theta_{i,j}) \rangle$ values closer to -1 , darker red colors correspond to values closer to $+1$. C) Toluene Newton plot without filtering. D), E) Toluene Newton plots with filtering on the relative angular distribution for the angular range indicated above each panel.

corresponding Newton plots for cases where preferably neighboring carbon ions were selected as reference ions i, j are shown in panels D) and F). Comparing these two cases reveals three major differences. First, gating on the respective regions of relative emission directions indeed selects predominantly (even in the experiment) alternating or neighboring carbon ions in the molecule. The momentum of the first reference ion is located by definition at $p_x > 0$ a.u., $p_y = 0$ a.u., and $p_z = 0$ a.u. Consequently, we do not observe intensity in the Newton plots in the region of $p_x > 200$ a.u. Similarly, depending on the gate, distinct parts of the intensity in the (p_x/p_y) -plane are missing, which belong to either the neighboring carbon in panel F) or to one carbon next to the neighboring one in the alternating case in panel E). Furthermore, as expected for the non-planar chair conformation of the molecule, we observe more defined contributions in the (p_x/p_z) -plane at $p_z > 200$ a.u. and $p_z < -200$ a.u., which is in line with an intuitive picture of the Coulomb explosion in a reference frame given by alternating carbons. The subtle peak at the center of the (p_y/p_z) -plane in Fig. 4D) and F) maps to the carbon atoms located in the same plane as the reference ions while emitted anti-parallel to one of them.

3.4.1 Molecular-frame angular emission distributions in spherical coordinates

Although the above discussion demonstrates that selecting events based on the reference ions' relative emission angles constructs

different Newton plots, the differences between the reference selections are subtle in the case of CHT, and mapping the features to the carbon sites is difficult. However, since all the emitted C^{2+} ions from CHT are nearly equal in their kinetic energy, all the features in the Newton plot for this molecule lie on the surface of a spherical shell, and the data can thus be represented in form of molecular-frame angular emission distributions in spherical coordinates, with only minor loss of information when projecting over the radial coordinate. The same approach has previously been used to visualize the Coulomb explosion of the heterocyclic thiophenone molecule⁷ and to trace the time-dependent evolution of a thionucleobasis after UV excitation²⁴ using time-resolved CEI.

Figure 5 shows such angular distributions in polar (θ) and azimuthal angle (ϕ) coordinates for the case of CHT. The simulated data are depicted in the top row (panels A-C) and the measured data in the middle row (panels D-F). The definition of the spherical coordinates is illustrated in Fig. 5G. Although this representation typically does not provide an intuitive image of the molecular geometry, the dimensionality reduction of the fragmentation enables a more effective mapping of features to specific carbon sites in the molecule, as we demonstrate below.

Panels A) and D) show the simulated and measured angular distributions without any filtering of the data. When filtering the data such that the reference ions are preferably given by alternating carbon atoms, we obtain the results shown in Figs. 5B) and

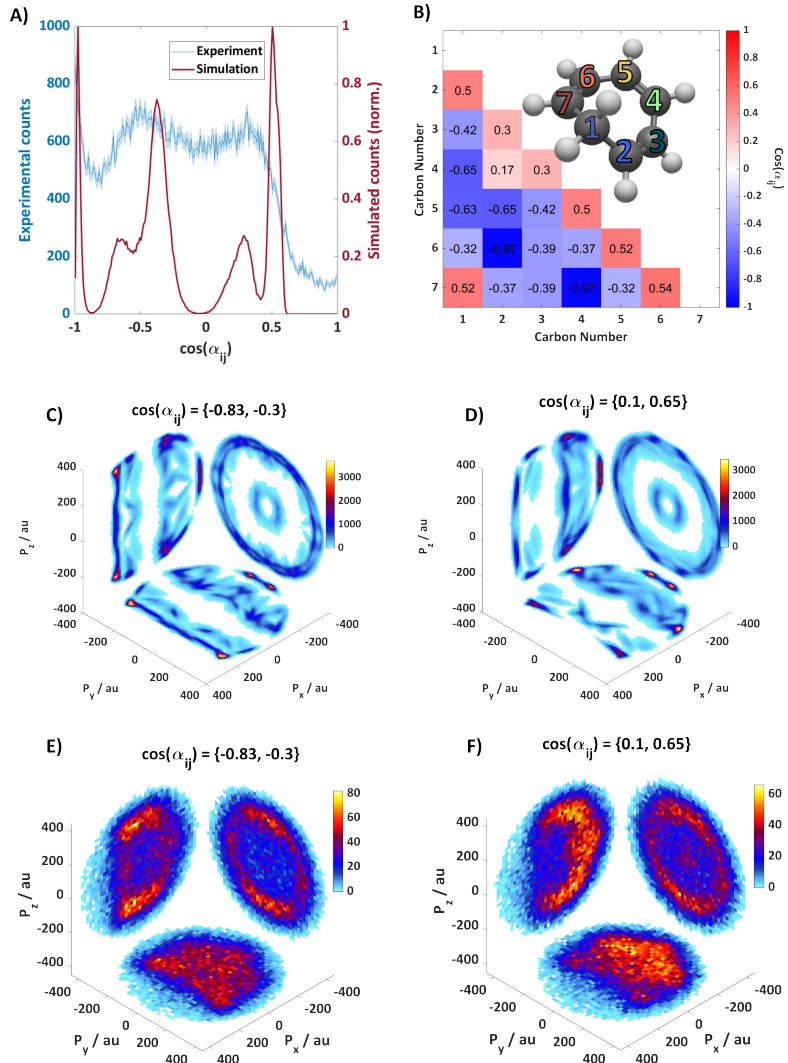


Fig. 4 Data filtering on angular correlations of the reference ions employed for defining the recoil frame of the cycloheptatriene Newton plots, similar to Fig. 3, which shows the same for toluene. A) Simulated (red) and experimental (blue) distribution of the relative emission angle of the two ions i and j used to define the recoil frame. B) Matrix showing the average $\langle \cos(\theta_{i,j}) \rangle$ in the simulated datasets for different combinations of carbon ions. C) and D) Simulated Newton plots filtered on the peaks in panel A) corresponding to alternating and neighboring carbons, respectively, selected by angular gating on the range of $\langle \cos(\theta_{i,j}) \rangle = (-0.83, -0.3)$ and $(0.1, 0.65)$, respectively. E) and F) Corresponding experimental results for the same angular gating as in panels C) and D).

5E). A prominent band appears at $\phi \approx 0.38\pi$ in both experiment and simulation. This peak corresponds to the emission feature of the carbon atom located between the two reference ions (i.e., if $i = 3$ and $j = 5$, then this peak maps C4). For the case where neighboring carbon atoms are selected as reference ions, we obtain the molecular-frame angular distributions shown in Figs. 5C and 5F). There, the band near $\phi \approx 0.38\pi$ occurs when the emitted atom is located near the reference ions, specifically the one closest to reference j (e.g., if $i = 5$ and $j = 4$, this maps C6). Lastly, signatures of the emission from the opposite side of the ring relative to the reference ions map to the peaks near $\phi \approx -0.63\pi$ and $\phi \approx \pi$, depending on the i, j reference permutation. For example, if $i = 3$ and $j = 4$ are chosen, then the peak occurs at $\phi \approx -0.63\pi$ and corresponds to carbon C7. When flipping the reference ions to $i = 4$ and $j = 3$, this carbon site is mapped to an angle of $\phi \approx \pi$.

For comparison, Figs. 5H and 5I show the simulated Newton

plots and angular emission distributions, respectively, for an idealized recoil frame defined by carbons C1 and C3, as illustrated in Fig. 5G), which represents one of the contributions to panels B) and E). Panel I) is asymmetric in $\cos(\theta)$, while the distributions shown in panels B) and E) are symmetric. A symmetric distribution in panel I) would occur if, in addition, the results for reference ions $i = 1$ and $j = 6$ (which corresponds to a rotation of the molecule sketched in panel G) around the p_x -axis) were superimposed. With this in mind, the measured and simulated angular distributions shown in panels E) and B) become intuitively understandable, and different regions can indeed be assigned to certain carbon sites in the molecule.

3.5 1,6-heptadiyne

Finally, for the non-cyclic isomer 1,6-heptadiyne, the single bonds that bridge different groups within the molecule allow for an easy

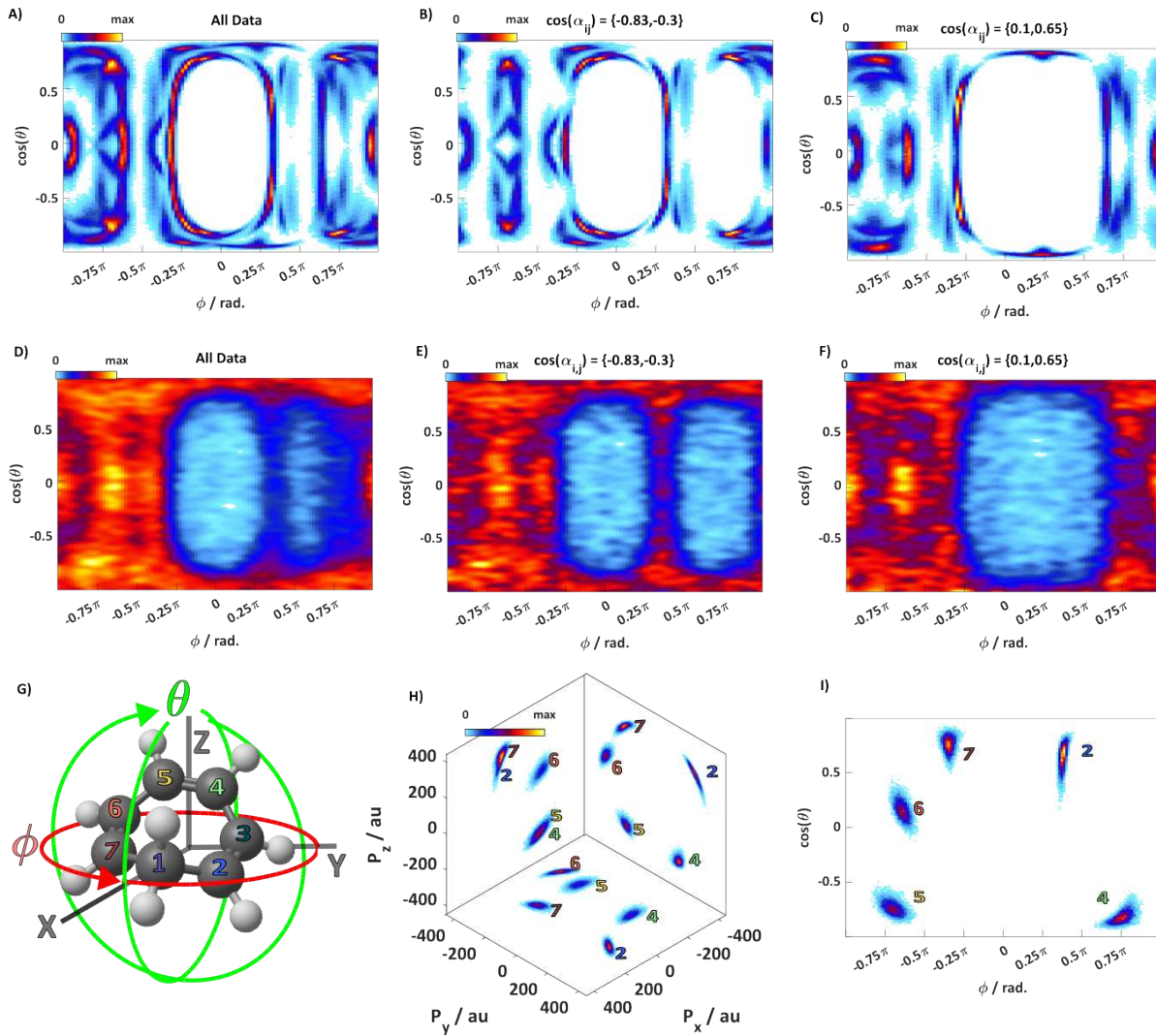


Fig. 5 Molecular-frame angular emission distributions in spherical coordinates for cycloheptatriene. The plots show the emission directions of ions (in the same molecular frame of reference as before) as a function of the polar (θ) and azimuthal (ϕ) angles for certain ranges of the relative angle α_{ij} , similar to Fig. 4. Simulated data are shown in the top row, panels A)-C), measured data in the middle row, panels D)-F). G) Definition of the spherical coordinates. H) Simulated Newton plot for a recoil frame defined by only $i = 1$ and $j = 3$. I) Simulated molecular-frame angular distribution for this idealized recoil-frame definition.

interconversion between different conformer geometries, with two conformers, GG-trans and AG, expected to be dominant.⁵⁴ The geometries of these two primary conformers are shown in Fig. 6 together with simulated Newton plots that were generated using ions $i = 1$ and $j = 6$ as references for the coordinate frame. The two Newton plots demonstrate that the simulated momentum distributions of the GG-trans and AG conformers look distinctly different when constructing the Newton plots using a well-defined reference frame. However, they still do not directly map to an intuitive picture of the molecular geometry. Comparing these results to the case of having arbitrary reference ions, as shown in Fig. 1I), and, in particular, to the corresponding measured results in Fig. 1F) indicates that in the case of 1,6-heptadiene, further information present in the CEI data need to be evaluated in order to discriminate molecular structures. Thus, in the following subsection, we inspect the measured proton momenta with the goal of using them as messengers of the molec-

ular structure, as successfully applied in our recent work on the Coulomb explosion of thiophenone and thiouracil^{7,24}.

3.6 Molecular-frame angular emission distributions of protons

We have shown above how Newton plots of the carbon atoms can be used to distinguish between the different C_7H_8 isomers and how their relative momentum distributions in the recoil frame can provide information on the geometric properties of these hydrocarbon molecules. We now turn to the H^+ ion momentum distributions and show that they also contain rich structural information, which complements the information encoded in the carbon ions and, when combined, provides additional metrics for distinguishing the structures. The experimental and simulated molecular-frame angular distributions of the H^+ fragments are shown in Fig. 7 for all three isomers, toluene, cycloheptatriene, and 1,6-heptadiyne. These plots are made by selecting the three-

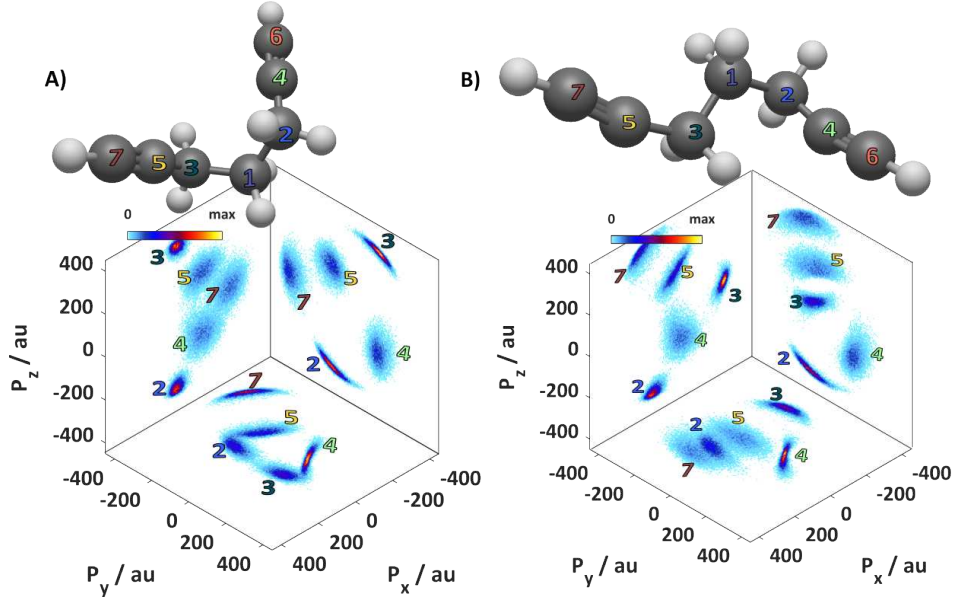


Fig. 6 Two expected conformer geometries of the 1,6-heptadiyne molecule, (a) GG-trans and (b) AG, along with the corresponding simulated Newton plots plotted with carbons C1 and C6 as reference ions.

particle coincidence channel $\text{H}^+ + \text{C}^{2+} + \text{C}^{2+}$ and using the two C^{2+} fragments to define the recoil frame in the same way as for the corresponding plots in the previous figures. The corresponding 3D Newton plots for the $\text{H}^+, \text{C}^{2+}, \text{C}^{2+}$ channel for all three isomers are shown in Fig. 5 of the Supplementary Material.

For the case of toluene, the majority of the protons are emitted in the plane spanned by the momenta of the $\text{C}^{2+} + \text{C}^{2+}$ reference ions (as evidenced by the peaks centered around $\cos \theta \approx 0$). The corresponding plots for cycloheptatriene in panels B) and D) demonstrate that for this nonplanar molecule, the H^+ ion emission also has an additional, strong out-of-plane component located near $\cos(\theta) \approx \pm 1$. Such contributions far from $\cos \theta \approx 0$ are even more pronounced for 1,6-heptadiyne, as shown in panels C) and E). For the sake of clarity, the simulated angular distributions for both the GG-trans and AG conformers of 1,6-heptadiyne, corresponding to the geometries sketched in Fig. 6, are shown.

Note that in the angular distributions for all isomers, the bright spot at the center of the plot corresponds to the H^+ originating from the hydrogen connected to one of the reference carbons.

The visually clear differences between the molecular-frame angular distributions of H^+ ions for all three isomers demonstrate that the H^+ ion momentum distributions are particularly well suited to distinguish isomers, as also shown recently for the case of the heterocyclic molecule thiophenone⁷, and that changes in the H^+ emission pattern can thus be used as reporters for subtle changes in the carbon backbone of the molecule²⁴.

4 Conclusions

We have investigated the prospects of X-ray-induced CEI of pure hydrocarbons, in which there is no preferential absorption site, nor can a unique recoil frame be defined for the interpretation of the CEI data, as there are no unique atomic sites in the molecule that can act as references for the momenta of other ions. Despite

the absence of such unique atomic markers, the measured momentum correlation patterns show discernible differences among the three isomers. For example, the toluene breakup yields a more structured Newton plot with multiple high-momentum ions arranged in a ring-like pattern reflecting the planar ring geometry, and a low-momentum feature near the origin, which can be attributed to the carbon nearest to the methyl group, whose emission is obstructed by the opposing repulsion from the neighboring carbon atoms. The cycloheptatriene momentum distribution is broader and less obviously reflective of a ring, with significant out-of-plane momentum components, consistent with the non-planar “chair” geometry of CHT. Finally, 1,6-heptadiyne, which can adopt many conformations, produces an almost homogeneous and isotropic carbon ion momentum distribution as a result of the ‘floppiness’ of the molecule.

Furthermore, by examining hydrogen ion (H^+) momentum distributions in coincidence with two C_2^+ ions, we observe that in the case of toluene, the H^+ ions are preferentially ejected within the plane of the benzene ring, whereas for cycloheptatriene and especially 1,6-heptadiyne, the H^+ ion momentum distributions exhibit much stronger components out of the plane spanned by the two reference ions – consistent with the non-planarity and conformational flexibility of those molecules.

By comparison to classical Coulomb explosion simulations, we can assign specific features in the Newton plots and molecular-frame angular emission distributions to specific molecular sites. For example, in toluene, the low-momentum central peak corresponds to the ring carbon bonded to the CH_3 group (experiencing opposing Coulomb forces from both the methyl group and the rest of the ring), whereas the outer-ring momentum peaks correspond to carbons on the benzene ring and the methyl carbon itself. By filtering events based on the relative angle between two C_2^+ fragment momenta and excluding low-kinetic-energy reference ions,

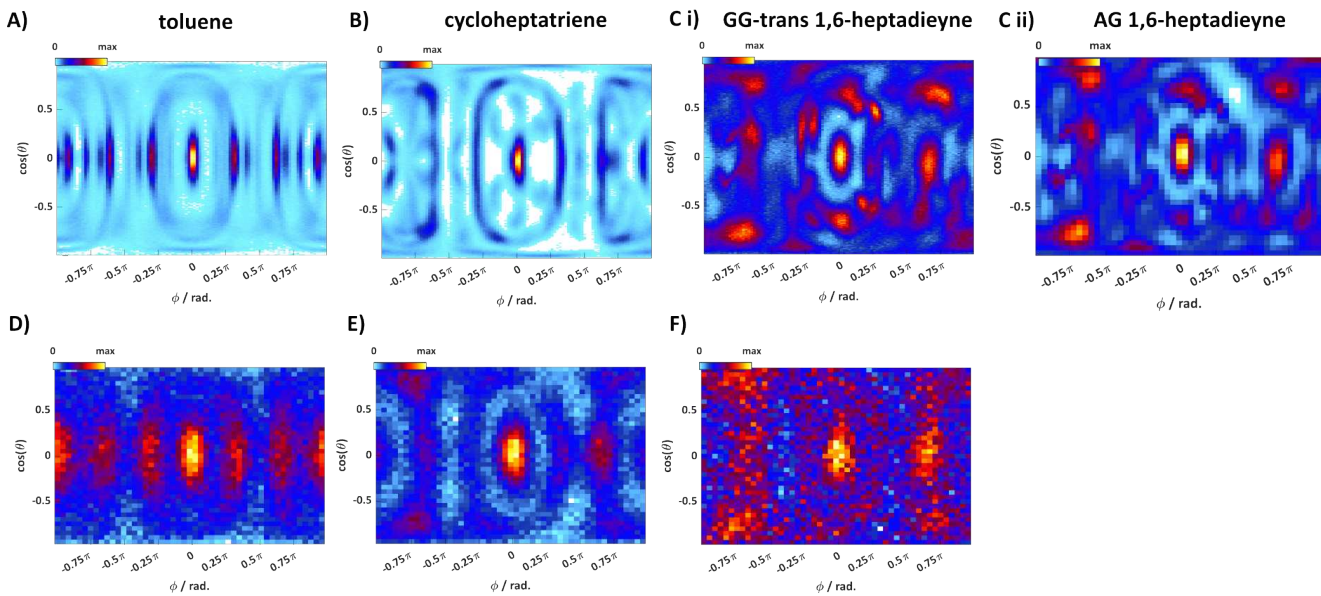


Fig. 7 Molecular-frame angular distributions of the emitted H^+ ions obtained from the $\text{H}^+ + \text{C}^{2+} + \text{C}^{2+}$ coincidence channel, with the two C^{2+} ions defining the recoil frame. A)-C): Simulation and D)-F) experimental data for toluene, cycloheptatriene, and 1,6-heptadiyne, respectively. Simulations for both the GG-trans and the AG conformers of 1,6-heptadiyne are shown in panels C i) and C ii), respectively.

we can isolate subsets of data associated with particular pairs of originating carbon sites. This filtering simplifies and 'cleans up' the momentum maps by reducing the contributing reference-frame combinations, making the correspondence to the molecular structure more evident.

Since the selection of these subsets degrades the statistics of the resulting Newton plots, the next generation of high-repetition-rate sources, both table-top and XFELs, will significantly improve the applicability of this selection method. We also expect the clarity of the correlation plots to improve as higher-order coincidence events can be analyzed, which reduces the uncertainty regarding the overall charge state of the molecule that leads, in parts, to the broad width of the measured energy and angular distributions.

Another avenue to reduce the ambiguity of the molecular reference frames for certain suitable molecules, such as toluene, could be isotope labeling, either by deuterium tagging or by replacing one of the carbon atoms with a carbon-13 isotope. However, depending on the spectrometer geometry and extraction voltages used for the experiment, it is typically not straightforward to separate highly energetic carbon ions with only one atomic mass unit difference as their time-of-flight peaks strongly overlap. This problem is alleviated in the case of 'complete' coincidences, i.e., for events where *all* fragment ions are detected, because momentum conservation between the emitted ions leads to narrow coincidence lines that allow for high mass resolution. Currently, the highest-order multi-ion coincidence momentum imaging results that we are aware of are for 8-ion coincidences recorded with a 3-kHz femtosecond laser³², but high-repetition-rate XFELs and high-power table-top femtosecond laser sources with repetition rates of 100 kHz or more are now available, suggesting that 'complete' coincidences may be achievable even for molecules with more than 10 atomic constituents.

Overall, the present study demonstrates that even without heavy atoms and unique markers, multi-ion coincidence CEI can still provide site-specific signatures of atomic positions (e.g., identifying which carbon was obstructed in toluene, or differences in hydrogen emission patterns), thereby distinguishing structural isomers. In future studies, machine learning tools and neural networks can be applied to the analysis of CEI data to help differentiating isomers formed as competing reaction products in a photochemical reaction³² and reconstructing their real-space molecular structure^{43,55}. New technical developments with regard to both experimental capabilities and data analysis therefore continue to lead to much improved capabilities, making CEI a promising candidate for time-resolved studies of ultrafast structural rearrangements (such as isomerization reactions) in pure hydrocarbons.

Author Contributions

AR and RB conceived the experiment, following initial discussions with DRo, MC, and PMW. The experiment was carried out by KDB, RB, TMB, SB, KC, BE, ADF, MI, EK, HVSL, XL, TMA, MM, TMu, SP, DRi, PS, FT, SU, ASV, EW, TJ, and DRo, with remote participation of MC, RF, LM, JPFN, AO, PMW, and AR. KDB analyzed the data, with help and guidance from RB, TJ, AR, and DRo. KB, RB, TJ, AR, and DRo interpreted the results and wrote the manuscript with input from all authors.

Conflicts of Interest

There are no conflicts to declare.

Data Availability

Data recorded for the experiment at the European XFEL are available at <https://doi.org/10.22003/XFEL.EU-DATA-002448-00>.

Acknowledgements

We acknowledge the European XFEL in Schenefeld, Germany, for the provision of X-ray free-electron laser beamtime at the SQS instrument through proposal no. 2448 and thank the EuXFEL staff for their assistance. This work was primarily supported by the Chemical Sciences, Geosciences, and Biosciences Division, Office of Basic Energy Sciences, Office of Science, US Department of Energy, who funded KDB, MC, KC, AO, AR, and DRo through grant no. DE-SC0020276, and HVSL, SP, and EW through grant no. DE-FG02-86ER13491. XL and RF were supported by the Linac Coherent Light Source (LCLS), SLAC National Accelerator Laboratory, which is funded by the U.S. Department of Energy, Office of Science, Office of Basic Energy Sciences under Contract No. DE-AC02-76SF00515. ASV was supported by the National Science Foundation grant no. PHYS-2409365. PMW and LM acknowledge support by the National Science Foundation grant no. CHE-2309434. FT acknowledges funding by the Deutsche Forschungsgemeinschaft (DFG, German Research Foundation) - Project 509471550, Emmy Noether Program. MI was partly supported by the Bundesministerium für Bildung und Forschung (BMBF) under grant 13K22CHA. MI and MM acknowledges support by the Cluster of Excellence 'Advanced Imaging of Matter' of the DFG—EXC 2056 and project ID 390715994.

Notes and references

- 1 Z. Vager, R. Naaman and E. P. Kanter, *Science*, 1989, **244**, 426–431.
- 2 M. Pitzer, M. Kunitski, A. S. Johnson, T. Jahnke, H. Sann, F. Sturm, L. P. H. Schmidt, H. Schmidt-Bocking, R. Dörner, J. Stohner, J. Kiedrowski, M. Reggelin, S. Marquardt, A. Schiesser, R. Berger and M. S. Schöffler, *Science*, 2013, **341**, 1096–1100.
- 3 R. Boll, J. M. Schäfer, B. Richard, K. Fehre, G. Kastirke, Z. Jurk, M. S. Schöffler, M. M. Abdullah, N. Anders, T. M. Baumann, S. Eckart, B. Erk, A. De Fanis, R. Dörner, S. Grundmann, P. Grychtol, A. Hartung, M. Hofmann, M. Ilchen, L. Inhester, C. Janke, R. Jin, M. Kircher, K. Kubicek, M. Kunitski, X. Li, T. Mazza, S. Meister, N. Melzer, J. Montano, V. Music, G. Nalin, Y. Ovcharenko, C. Passow, A. Pier, N. Rennhack, J. Rist, D. E. Rivas, D. Rolles, I. Schlichting, L. P. H. Schmidt, P. Schmidt, J. Siebert, N. Strenger, D. Trabert, F. Trinter, I. Vela-Perez, R. Wagner, P. Walter, M. Weller, P. Ziolkowski, S.-K. Son, A. Rudenko, M. Meyer, R. Santra and T. Jahnke, *Nature Physics*, 2022, **18**, 423–428.
- 4 S. Bhattacharyya, K. Borne, F. Ziaeef, S. Pathak, E. Wang, A. S. Venkatachalam, X. Li, N. Marshall, K. D. Carnes, C. W. Fehrenbach, T. Severt, I. Ben-Itzhak, A. Rudenko and D. Rolles, *The Journal of Physical Chemistry Letters*, 2022, **13**, 5845–5853.
- 5 X. Li, A. Rudenko, M. S. Schöffler, N. Anders, T. M. Baumann, S. Eckart, B. Erk, A. De Fanis, K. Fehre, R. Dörner, L. Foucar, S. Grundmann, P. Grychtol, A. Hartung, M. Hofmann, M. Ilchen, C. Janke, G. Kastirke, M. Kircher, K. Kubicek, M. Kunitski, T. Mazza, S. Meister, N. Melzer, J. Montano, V. Music, G. Nalin, Y. Ovcharenko, C. Passow, A. Pier, N. Rennhack, J. Rist, D. E. Rivas, I. Schlichting, L. P. H. Schmidt, P. Schmidt, J. Siebert, N. Strenger, D. Trabert, F. Trinter, I. Vela-Perez, R. Wagner, P. Walter, M. Weller, P. Ziolkowski, D. Rolles, M. Meyer, T. Jahnke and R. Boll, *Physical Review Research*, 2022, **4**, 013029.
- 6 H. V. S. Lam, A. S. Venkatachalam, S. Bhattacharyya, K. Chen, K. Borne, E. Wang, R. Boll, T. Jahnke, V. Kumarappan, A. Rudenko and D. Rolles, *Physical Review Letters*, 2024, **132**, 123201.
- 7 A. Green, K. Chen, S. Bhattacharyya, F. Allum, S. Usenko, M. Ashfold, T. Baumann, K. Borne, M. Brouard, M. Burt, B. Curchod, B. Erk, R. Forbes, L. Ibele, R. Ingle, H. Lam, X. Li, K. Lin, T. Mazza, J. McManus, M. Meyer, T. Mullins, J. Figueira Nunes, D. Rivas, A. Roerig, A. Rouzee, P. Schmidt, J. Searles, B. Senffleben, H. Stapelfeldt, R. Tanyag, F. Trinter, A. Venkatachalam, E. Wang, E. Warne, P. Weber, T. Wolf, T. Jahnke, A. Rudenko, R. Boll and D. Rolles, *Journal of the American Chemical Society*, 2025, **147**, 37133–37143.
- 8 H. V. S. Lam, V.-H. Hoang, A. S. Venkatachalam, S. Bhattacharyya, K. Chen, S. Jacob, S. Kudagama, T. T. Nguyen, D. Rolles, U. Thumm, A. Rudenko and V. Kumarappan, *Physical Review A*, 2025, **111**, L061101.
- 9 W. Zhou, L. Ge, G. A. Cooper, S. W. Crane, M. H. Evans, M. N. R. Ashfold and C. Vallance, *The Journal of Chemical Physics*, 2020, **153**, 184201.
- 10 D. S. Gemmell, *Chemical Reviews*, 1980, **80**, 301–311.
- 11 P. Herwig, D. Schwalm, M. Čížek, R. Golser, M. Grieser, O. Heber, R. Repnow, A. Wolf and H. Kreckel, *Physical Review A*, 2013, **87**, 062513.
- 12 N. Neumann, D. Hant, L. P. H. Schmidt, J. Titze, T. Jahnke, A. Czasch, M. S. Schöffler, K. Kreidi, O. Jagutzki, H. Schmidt-Bocking and R. Dörner, *Physical Review Letters*, 2010, **104**, 103201.
- 13 L. P. H. Schmidt, T. Jahnke, A. Czasch, M. Schöffler, H. Schmidt-Bocking and R. Dörner, *Physical Review Letters*, 2012, **108**, 073202.
- 14 E. Wang, X. Shan, L. Chen, T. Pfeifer, X. Chen, X. Ren and A. Dorn, *The Journal of Physical Chemistry A*, 2020, **124**, 2785–2791.
- 15 H. Yuan, Y. Gao, B. Yang, S. Gu, H. Lin, D. Guo, J. Liu, S. Zhang, X. Ma and S. Xu, *Physical Review Letters*, 2024, **133**, 193002.
- 16 H. Stapelfeldt, E. Constant, H. Sakai and P. B. Corkum, *Physical Review A*, 1998, **58**, 426–433.
- 17 C. A. Schouder, A. S. Chatterley, J. D. Pickering and H. Stapelfeldt, *Annual Review of Physical Chemistry*, 2022, **73**, 323–347.
- 18 S. W. Crane, J. W. Lee, M. N. Ashfold and D. Rolles, *Physical Chemistry Chemical Physics*, 2023, **25**, 16672–16698.
- 19 A. Hishikawa, A. Matsuda, M. Fushitani and E. J. Takahashi, *Physical Review Letters*, 2007, **99**, 258302.
- 20 T. Endo, S. P. Neville, V. Wanie, S. Beaulieu, C. Qu, J. Deschamps, P. Lassonde, B. E. Schmidt, H. Fujise, M. Fushitani, A. Hishikawa, P. L. Houston, J. M. Bowman, M. S. Schuurman, F. Légaré and H. Ibrahim, *Science*, 2020, **370**, 1072–1077.

21 M. McDonnell, A. C. LaForge, J. Reino-González, M. Disla, N. G. Kling, D. Mishra, R. Obaid, M. Sundberg, V. Svoboda, S. Díaz-Tendero, F. Martín and N. Berrah, *The Journal of Physical Chemistry Letters*, 2020, **11**, 6724–6729.

22 M. Pitzer, G. Kastirke, M. Kunitski, T. Jahnke, T. Bauer, C. Goihl, F. Trinter, C. Schober, K. Henrichs, J. Becht, S. Zeller, H. Gassert, M. Waitz, A. Kuhlins, H. Sann, F. Sturm, F. Wiegandt, R. Wallauer, L. P. H. Schmidt, A. S. Johnson, M. Mazenauer, B. Spenger, S. Marquardt, S. Marquardt, H. Schmidt-Böcking, J. Stohner, R. Dörner, M. Schöffler and R. Berger, *ChemPhysChem*, 2016, **17**, 2465–2472.

23 U. Ablikim, C. Bomme, H. Xiong, E. Saveliev, R. Obaid, B. Kaderiya, S. Augustin, K. Schnorr, I. Dumitriu, T. Osipov, R. Bilodeau, D. Kilcoyne, V. Kumarappan, A. Rudenko, N. Berrah and D. Rolles, *Scientific Reports*, 2016, **6**, 38202.

24 T. Jahnke, S. Mai, S. Bhattacharyya, K. Chen, R. Boll, M. E. Castellani, S. Dold, U. Frühling, A. E. Green, M. Ilchen, R. Ingle, G. Kastirke, H. V. S. Lam, F. Lever, D. Mayer, T. Mazza, T. Mullins, Y. Ovcharenko, B. Senftleben, F. Trinter, Atia-Tul-Noor, S. Usenko, A. S. Venkatachalam, A. Rudenko, D. Rolles, M. Meyer, H. Ibrahim and M. Gühr, *Nature Communications*, 2025, **16**, 2074.

25 X. Li, R. Boll, P. Vindel-Zandbergen, J. González-Vázquez, D. E. Rivas, S. Bhattacharyya, K. Borne, K. Chen, A. De Fannis, B. Erk *et al.*, *Nature Communications*, 2025, **16**, 7006.

26 L. Christensen, J. H. Nielsen, C. B. Brandt, C. B. Madsen, L. B. Madsen, C. S. Slater, A. Lauer, M. Brouard, M. P. Johansson, B. Shepperson and H. Stapelfeldt, *Physical Review Letters*, 2014, **113**, 073005.

27 K. Amini, E. Saveliev, F. Brauße, N. Berrah, C. Bomme, M. Brouard, M. Burt, L. Christensen, S. Düsterer, B. Erk, H. Höppner, T. Kierspel, F. Krecinic, A. Lauer, J. W. L. Lee, M. Müller, E. Müller, T. Mullins, H. Redlin, N. Schirmel, J. Thøgersen, S. Techert, S. Toleikis, R. Treusch, S. Trippel, A. Ulmer, C. Vallance, J. Wiese, P. Johnsson, J. Küpper, A. Rudenko, A. Rouzée, H. Stapelfeldt, D. Rolles and R. Boll, *Structural Dynamics*, 2018, **5**, 014301.

28 J. D. Pickering, K. Amini, M. Brouard, M. Burt, I. J. Bush, L. Christensen, A. Lauer, J. H. Nielsen, C. S. Slater and H. Stapelfeldt, *The Journal of Chemical Physics*, 2016, **144**, 161105.

29 M. Burt, R. Boll, J. W. Lee, K. Amini, H. Köckert, C. Vallance, A. S. Gentleman, S. R. Mackenzie, S. Bari, C. Bomme *et al.*, *Physical Review A*, 2017, **96**, 043415.

30 F. Allum, M. Burt, K. Amini, R. Boll, H. Köckert, P. K. Olshin, S. Bari, C. Bomme, F. Brauße, B. Cunha de Miranda, S. Düsterer, B. Erk, M. Géléoc, R. Geneaux, A. S. Gentleman, G. Goldsztejn, R. Guillemin, D. M. P. Holland, I. Ismail, P. Johnsson, L. Journel, J. Küpper, J. Lahl, J. W. L. Lee, S. Maclot, S. R. Mackenzie, B. Manschwetus, A. S. Mereshchenko, R. Mason, J. Palaudoux, M. N. Piancastelli, F. Penent, D. Rompotis, A. Rouzée, T. Ruchon, A. Rudenko, E. Saveliev, M. Simon, N. Schirmel, H. Stapelfeldt, S. Techert, O. Travnikova, S. Trippel, J. G. Underwood, C. Vallance, J. Wiese, F. Ziaeef, M. Brouard, T. Marchenko and D. Rolles, *The Journal of Chemical Physics*, 2018, **149**, 204313.

31 C. Cheng, L. J. Frasinski, G. Moğol, F. Allum, A. J. Howard, D. Rolles, P. H. Bucksbaum, M. Brouard, R. Forbes and T. Weinacht, *Physical Review Letters*, 2023, **130**, 093001.

32 A. S. Venkatachalam, L. Greenman, J. Stallbaumer, A. Rudenko, D. Rolles and H. V. S. Lam, *Nature Communications*, 2025, **16**, 11366.

33 B. Richard, R. Boll, S. Banerjee, J. M. Schäfer, Z. Jurek, G. Kastirke, K. Fehre, M. S. Schöffler, N. Anders, T. M. Baumann, S. Eckart, B. Erk, A. D. Fanis, R. Dörner, S. Grundmann, P. Grychtol, M. Hofmann, M. Ilchen, M. Kircher, K. Kubicek, M. Kunitski, X. Li, T. Mazza, S. Meister, N. Melzer, J. Montano, V. Music, Y. Ovcharenko, C. Passow, A. Pier, N. Rennhack, J. Rist, D. E. Rivas, D. Rolles, I. Schlichting, L. P. H. Schmidt, P. Schmidt, D. Trabert, F. Trinter, R. Wagner, P. Walter, P. Ziolkowski, A. Rudenko, M. Meyer, R. Santra, L. Inhester and T. Jahnke, *Science*, 2025, **389**, 650–654.

34 S. Pathak, R. Obaid, S. Bhattacharyya, J. Bürger, X. Li, J. Tross, T. Severt, B. Davis, R. C. Bilodeau, C. A. Trallero-Herrero, A. Rudenko, N. Berrah and D. Rolles, *The Journal of Physical Chemistry Letters*, 2020, **11**, 10205–10211.

35 J. L. Hansen, J. H. Nielsen, C. B. Madsen, A. T. Lindhardt, M. P. Johansson, T. Skrydstrup, L. B. Madsen and H. Stapelfeldt, *The Journal of Chemical Physics*, 2012, **136**, 204310.

36 E. Wang, S. Bhattacharyya, K. Chen, K. Borne, S. Pathak, H. V. S. Lam, A. S. Venkatachalam, X. Chen, R. Boll, T. Jahnke, A. Rudenko and D. Rolles, <https://arxiv.org/abs/2311.05099>, 2023.

37 M. Miniti, J. Budarz, A. Kirrander, J. Robinson, D. Ratner, T. Lane, D. Zhu, J. Glownia, M. Kozina, H. Lemke, M. Sikorski, Y. Feng, S. Nelson, K. Saita, B. Stankus, T. Northey, J. Hastings and P. Weber, *Physical Review Letters*, 2015, **114**, 255501.

38 T. J. A. Wolf, D. M. Sanchez, J. Yang, R. M. Parrish, J. P. F. Nunes, M. Centurion, R. Coffee, J. P. Cryan, M. Gühr, K. Hegazy, A. Kirrander, R. K. Li, J. Ruddock, X. Shen, T. Vecchione, S. P. Weathersby, P. M. Weber, K. Wilkin, H. Yong, Q. Zheng, X. J. Wang, M. P. Miniti and T. J. Martínez, *Nature Chemistry*, 2019, **11**, 504–509.

39 J. M. Ruddock, H. Yong, B. Stankus, W. Du, N. Goff, Y. Chang, A. Odate, A. M. Carrascosa, D. Bellshaw, N. Zotev, M. Liang, S. Carbo, J. Koglin, J. S. Robinson, S. Boutet, A. Kirrander, M. P. Miniti and P. M. Weber, *Science Advances*, 2019, **5**, eaax6625.

40 J. H. Hubbell, W. J. Veigle, E. A. Briggs, R. T. Brown, D. T. Cromer and R. J. Howerton, *Journal of Physical and Chemical Reference Data*, 1975, **4**, 471–538.

41 M. Centurion, T. J. A. Wolf and J. Yang, *Annual Review of Physical Chemistry*, 2022, **73**, 21–42.

42 A. Moreno Carrascosa, H. Yong, D. L. Crittenden, P. M. Weber and A. Kirrander, *Journal of Chemical Theory and Computation*, 2019, **15**, 2836–2846.

43 X. Li, T. Jahnke, R. Boll, J. Han, M. Xu, M. Meyer, M. N. Piancastelli, D. Rolles, A. Rudenko, F. Trinter, T. J. A. Wolf, J. B. Thayer, J. P. Cryan, S. Ermont and P. J. Ho,

44 W. Decking, S. Abeghyan, P. Abramian, A. Abramsky, A. Aguirre, C. Albrecht, P. Alou, M. Altarelli, P. Altmann, K. Amyan, V. Anashin, E. Apostolov, K. Appel, D. Auguste, V. Ayvazyan, S. Baark, F. Babies, N. Baboi, P. Bak, V. Balandin, R. Baldinger, B. Baranasic, S. Barbanotti, O. Belikov, V. Belokurov, L. Belova, V. Belyakov, S. Berry, M. Bertucci, B. Beutner, A. Block, M. Blöcher, T. Böckmann, C. Bohm, M. Böhner, V. Bondar, E. Bondarchuk, M. Bonezzi, P. Borowiec, C. Bösch, U. Bösenberg, A. Bosotti, R. Böspflug, M. Bousonville, E. Boyd, Y. Bozhko, A. Brand, J. Branlard, S. Brieche, F. Brinker, S. Brinker, R. Brinkmann, S. Brockhauser, O. Brovko, H. Brück, A. Brüdgam, L. Butkowski, T. Büttner, J. Calero, E. Castro-Carballo, G. Cattalanotto, J. Charrier, J. Chen, A. Cherepenko, V. Cheskidov, M. Chiodini, A. Chong, S. Choroba, M. Chorowski, D. Churanov, W. Cichalewski, M. Clausen, W. Clement, C. Cloué, J. A. Cobos, N. Coppola, S. Cunis, K. Czuba, M. Czwalinna, B. D'Almagne, J. Dammann, H. Danared, A. de Zubiaurre Wagner, A. Delfs, T. Delfs, F. Dietrich, T. Dietrich, M. Dohlus, M. Dommach, A. Donat, X. Dong, N. Doynikov, M. Dressel, M. Duda, P. Duda, H. Eckoldt, W. Ehsan, J. Eidam, F. Eints, C. Engling, U. Englisch, A. Ermakov, K. Escherich, J. Eschke, E. Saldin, M. Faesing, A. Fallou, M. Felber, M. Fenner, B. Fernandes, J. M. Fernández, S. Feuker, K. Filippakopoulos, K. Floettmann, V. Fogel, M. Fontaine, A. Francés, I. F. Martin, W. Freund, T. Freyermuth, M. Friedland, L. Fröhlich, M. Fusetti, J. Fydrych, A. Gallas, O. García, L. Garcia-Tabares, G. Geloni, N. Gerasimova, C. Gerth, P. Geßler, V. Gharibyan, M. Gloor, J. Głowinkowski, A. Goessel, Z. Golebiewski, N. Golubeva, W. Grabowski, W. Graeff, A. Grebentsov, M. Grecki, T. Grevsmuehl, M. Gross, U. Grosse-Wortmann, J. Grünert, S. Grunewald, P. Grzegory, G. Feng, H. Guler, G. Gusev, J. L. Gutierrez, L. Hagge, M. Hamborg, R. Hanneken, E. Harms, I. Hartl, A. Hauberg, S. Hauf, J. Hauschmidt, J. Hauser, J. Havlicek, A. Hedqvist, N. Heidbrook, F. Hellberg, D. Henning, O. Hensler, T. Hermann, A. Hidvégi, M. Hierholzer, H. Hintz, F. Hoffmann, M. Hoffmann, M. Hoffmann, Y. Holler, M. Hüning, A. Ignatenko, M. Ilchen, A. İluk, J. Iversen, J. Iversen, M. Izquierdo, L. Jachmann, N. Jardon, U. Jastrow, K. Jensch, J. Jensen, M. Ježabek, M. Jidda, H. Jin, N. Johansson, R. Jonas, W. Kaabi, D. Kaefer, R. Kammering, H. Kapitza, S. Karabekyan, S. Karstensen, K. Kasprzak, V. Katalev, D. Keese, B. Keil, M. Kholopov, M. Killenberger, B. Kitaev, Y. Klimchenko, R. Klos, L. Knebel, A. Koch, M. Koepke, S. Köhler, W. Köhler, N. Kohlstrunk, Z. Konopkova, A. Konstantinov, W. Kook, W. Koprek, M. Körfer, O. Korth, A. Kosarev, K. Kosiński, D. Kostin, Y. Kot, A. Kotarba, T. Kozak, V. Kozak, R. Kramert, M. Krasilnikov, A. Krasnov, B. Krause, L. Kravchuk, O. Krebs, R. Kretschmer, J. Kreutzkamp, O. Kröplin, K. Krzysik, G. Kube, H. Kuehn, N. Kujala, V. Kulikov, V. Kuzminych, D. La Civita, M. Lacroix, T. Lamb, A. Lancetov, M. Larsson, D. Le Pinvidic, S. Lederer, T. Lensch, D. Lenz, A. Leuschner, F. Levenhagen, Y. Li, J. Liebing, L. Lilje, T. Limberg, D. Lipka, B. List, J. Liu, S. Liu, B. Lorbeer, J. Lorkiewicz, H. H. Lu, F. Ludwig, K. Machau, W. Maciocha, C. Madec, C. Maguer, C. Maiano, I. Maksimova, K. Malcher, T. Maltezopoulos, E. Mamoshkina, B. Manschwetus, F. Marcellini, G. Marinkovic, T. Martinez, H. Martirosyan, W. Maschmann, M. Maslov, A. Matheisen, U. Mavric, J. Meißner, K. Meissner, M. Messerschmidt, N. Meyners, G. Michalski, P. Michelato, N. Mildner, M. Moe, F. Moglia, C. Mohr, S. Mohr, W. Möller, M. Mommerz, L. Monaco, C. Montiel, M. Moretti, I. Morozov, P. Morozov, D. Mross, J. Mueller, C. Müller, J. Müller, K. Müller, J. Munilla, A. Münnich, V. Muratov, O. Napolis, B. Näser, N. Nefedov, R. Neumann, R. Neumann, N. Ngada, D. Noelle, F. Obier, I. Okuney, J. A. Oliver, M. Omet, A. Oppelt, A. Ottmar, M. Oublaid, C. Pagani, R. Paparella, V. Paramonov, C. Peitzmann, J. Penning, A. Perus, F. Peters, B. Petersen, A. Petrov, I. Petrov, S. Pfeiffer, J. Pflüger, S. Philipp, Y. Pienaud, P. Pierini, S. Pivovarov, M. Planas, E. Pławski, M. Pohl, J. Polinski, V. Popov, S. Prat, J. Prenting, G. Priebe, H. Pryschelski, K. Przygoda, E. Pyata, B. Racky, A. Rathjen, W. Ratuschni, S. Regnaud-Campderros, K. Rehlich, D. Reschke, C. Robson, J. Roever, M. Roggli, J. Rothenburg, E. Rusiński, R. Rybaniec, H. Sahling, M. Salmani, L. Samoylova, D. Sanzone, F. Saretzki, O. Sawlanski, J. Schaffran, H. Schlarb, M. Schlösser, V. Schlott, C. Schmidt, F. Schmidt-Foehre, M. Schmitz, M. Schmökel, T. Schnautz, E. Schneidmiller, M. Scholz, B. Schöneburg, J. Schultze, C. Schulz, A. Schwarz, J. Sekutowicz, D. Sellmann, E. Semenov, S. Serkez, D. Sertore, N. Shehzad, P. Shemarykin, L. Shi, M. Sienkiewicz, D. Sikora, M. Sikorski, A. Silenzi, C. Simon, W. Singer, X. Singer, H. Sinn, K. Sinram, N. Skvorodnev, P. Smirnow, T. Sommer, A. Sorokin, M. Stadler, M. Steckel, B. Steffen, N. Steinhau-Kühl, F. Stephan, M. Stodulski, M. Stolper, A. Sulimov, R. Susen, J. Świerblewski, C. Sydlo, E. Syresin, V. Sytchev, J. Szuba, N. Tesch, J. Thie, A. Thiebault, K. Tiedtke, D. Tischhauser, J. Tolkiehn, S. Tomin, F. Tonisch, F. Toral, I. Torbin, A. Trapp, D. Treyer, G. Trowitzsch, T. Trublet, T. Tschentscher, F. Ullrich, M. Vannoni, P. Varela, G. Varghese, G. Vashchenko, M. Vasic, C. Vazquez-Velez, A. Verguet, S. Vilcins-Czvitkovits, R. Villanueva, B. Visentin, M. Viti, E. Vogel, E. Volobuev, R. Wagner, N. Walker, T. Wamsat, H. Weddig, G. Weichert, H. Weise, R. Wenndorf, M. Werner, R. Wichmann, C. Wiebers, M. Wienczek, T. Wilksen, I. Will, L. Winkelmann, M. Winkowski, K. Wittenburg, A. Witzig, P. Wlk, T. Wohlenberg, M. Wojciechowski, F. Wolff-Fabris, G. Wrochna, K. Wrona, M. Yakopov, B. Yang, F. Yang, M. Yurkov, I. Zagorodnov, P. Zalden, A. Zavadtsev, D. Zavadtsev, A. Zhirnov, A. Zhukov, V. Ziemann, A. Zolotov, N. Zolotukhina, F. Zummack and D. Zybin, *Nature Photonics*, 2020, **14**, 391–397.

45 G. Kastirke, M. S. Schöffler, M. Weller, J. Rist, R. Boll, N. Anders, T. M. Baumann, S. Eckart, B. Erk, A. De Fanis, K. Fehre, A. Gatton, S. Grundmann, P. Grychtol, A. Hartung, M. Hofmann, M. Ilchen, C. Janke, M. Kircher, M. Kunitski, X. Li, T. Mazza, N. Melzer, J. Montano, V. Music, G. Nalin, Y. Ovcharenko, A. Pier, N. Rennhack, D. E. Rivas, R. Dörner, D. Rolles, A. Rudenko, P. Schmidt, J. Siebert, N. Strenger,

D. Trabert, I. Vela-Perez, R. Wagner, T. Weber, J. B. Williams, P. Ziolkowski, L. P. Schmidt, A. Czasch, K. Ueda, F. Trinter, M. Meyer, P. V. Demekhin and T. Jahnke, *Physical Review Letters*, 2020, **125**, 163201.

46 G. Kastirke, M. S. Schöffler, M. Weller, J. Rist, R. Boll, N. Anders, T. M. Baumann, S. Eckart, B. Erk, A. De Fanis, K. Fehre, A. Gatton, S. Grundmann, P. Grychtol, A. Hartung, M. Hofmann, M. Ilchen, C. Janke, M. Kircher, M. Kunitski, X. Li, T. Mazza, N. Melzer, J. Montano, V. Music, G. Nalin, Y. Ovcharenko, A. Pier, N. Rennhack, D. E. Rivas, R. Dörner, D. Rolles, A. Rudenko, P. Schmidt, J. Siebert, N. Strenger, D. Trabert, I. Vela-Perez, R. Wagner, T. Weber, J. B. Williams, P. Ziolkowski, L. P. H. Schmidt, A. Czasch, F. Trinter, M. Meyer, K. Ueda, P. V. Demekhin and T. Jahnke, *Physical Review X*, 2020, **10**, 021052.

47 T. Jahnke, R. Guillemin, L. Inhester, S.-K. Son, G. Kastirke, M. Ilchen, J. Rist, D. Trabert, N. Melzer, N. Anders, T. Mazza, R. Boll, A. De Fanis, V. Music, T. Weber, M. Weller, S. Eckart, K. Fehre, S. Grundmann, A. Hartung, M. Hofmann, C. Janke, M. Kircher, G. Nalin, A. Pier, J. Siebert, N. Strenger, I. Vela-Perez, T. Baumann, P. Grychtol, J. Montano, Y. Ovcharenko, N. Rennhack, D. Rivas, R. Wagner, P. Ziolkowski, P. Schmidt, T. Marchenko, O. Travnikova, L. Journel, I. Ismail, E. Kukk, J. Niskanen, F. Trinter, C. Vozzi, M. Devetta, S. Stagira, M. Gisselbrecht, A. Jäger, X. Li, Y. Malakar, M. Martins, R. Feifel, L. Schmidt, A. Czasch, G. Sansone, D. Rolles, A. Rudenko, R. Moshammer, R. Dörner, M. Meyer, T. Pfeifer, M. Schöffler, R. Santra, M. Simon and M. Piancastelli, *Physical Review X*, 2021, **11**, 041044.

48 J. Gruenert, M. Planas, F. Dietrich, T. Falk, W. Freund, A. Koch, N. Kujala, J. Laksman, J. Liu, T. Maltezopoulos, K. Tiedtke, U. Jastrow, A. Sorokin, E. Syresin, A. Grebentsov and O. Brovko, *Journal of Synchrotron Radiation*, 2019, **26**, 1422–1431.

49 T. Mazza, T. M. Baumann, R. Boll, A. De Fanis, P. Grychtol, M. Ilchen, J. Montaño, V. Music, Y. Ovcharenko, N. Rennhack, D. E. Rivas, A. Rörig, P. Schmidt, S. Usenko, P. Ziolkowski, D. La Civita, M. Vannoni, H. Sinn, B. Keitel, E. Plönjes, U. F. Jastrow, A. Sorokin, K. Tiedtke, K. Mann, B. Schäfer, N. Breckwoldt, S.-K. Son and M. Meyer, *Journal of Synchrotron Radiation*, 2023, **30**, 457–467.

50 M. D. Hanwell, D. E. Curtis, D. C. Lonie, T. Vandermeersch, E. Zurek and G. R. Hutchison, *Journal of Cheminformatics*, 2012, **4**, 17.

51 N. M. O'Boyle, M. Banck, C. A. James, C. Morley, T. Vandermeersch and G. R. Hutchison, *Journal of Cheminformatics*, 2011, **3**, 33.

52 M. Barbatti, M. Ruckenbauer, F. Plasser, J. Pittner, G. Granucci, M. Persico and H. Lischka, *WIREs Computational Molecular Science*, 2014, **4**, 26–33.

53 J. Eland, *Molecular Physics*, 1987, **61**, 725–745.

54 A. A. Restrepo and R. K. Bohn, *Journal of Molecular Structure*, 2007, **833**, 189–196.

55 A. Ghanaatian, A. K. Ravi, J. Stallbaumer, H. V. S. Lam, A. Rudenko, L. Greenman, N. Albin, D. Caragea and D. Rolles, *submitted*, 2025.

Supplementary Material for Probing the structure of cyclic hydrocarbon molecules with X-ray-induced Coulomb explosion imaging [†]

Kurtis D. Borne^{a,b}, Rebecca Boll^c, Thomas M. Baumann^c, Surjendu Bhattacharyya^{a,b}, Martin Centurion^d, Keyu Chen^a, Benjamin Erk^e, Alberto De Fanis^c, Ruaridh Forbes^{b,f}, Markus Ilchen^{c,e,g}, Edwin Kukk^h, Huynh V. S. Lam^a, Xiang Li^b, Lingyu Maⁱ, Tommaso Mazza^c, Michael Meyer^c, Terence Mullins^{c,e,l}, J. Pedro F. Nunes^d, Asami Odateⁱ, Shashank Pathak^a, Daniel Rivas^c, Philipp Schmidt^c, Florian Trinter^j, Sergey Usenko^c, Anbu S. Venkatachalam^a, Enliang Wang^{a,k}, Peter M. Weberⁱ, Till Jahnke^c, Artem Rudenko^a, and Daniel Rolles^{a,*}

USA

^a Deutsches Elektronen-Synchrotron DESY, Hamburg, Germany

^f Department of Chemistry, University of California, Davis, CA, USA

^g Department of Physics, University of Hamburg, Hamburg, Germany

^b Department of Physics and Astronomy, University of Turku, Turku, Finland

ⁱ Department of Chemistry, Brown University, Providence, RI, USA

^j Molecular Physics, Fritz-Haber-Institut der Max-Planck-Gesellschaft, Berlin, Germany

^k Hefei National Research Center for Physical Sciences at the Microscale and Department of Modern Physics, University of Science and Technology of China, Hefei, China

^l The Hamburg Centre for Ultrafast Imaging, Universität Hamburg, Hamburg, Germany

^a J. R. Macdonald Laboratory, Department of Physics, Kansas State University, Manhattan, KS, USA

^b Linac Coherent Light Source, SLAC National Accelerator Laboratory, Menlo Park, CA, USA

^c European XFEL, Schenefeld, Germany

^d Department of Physics and Astronomy, University of Nebraska–Lincoln, Lincoln, NE,

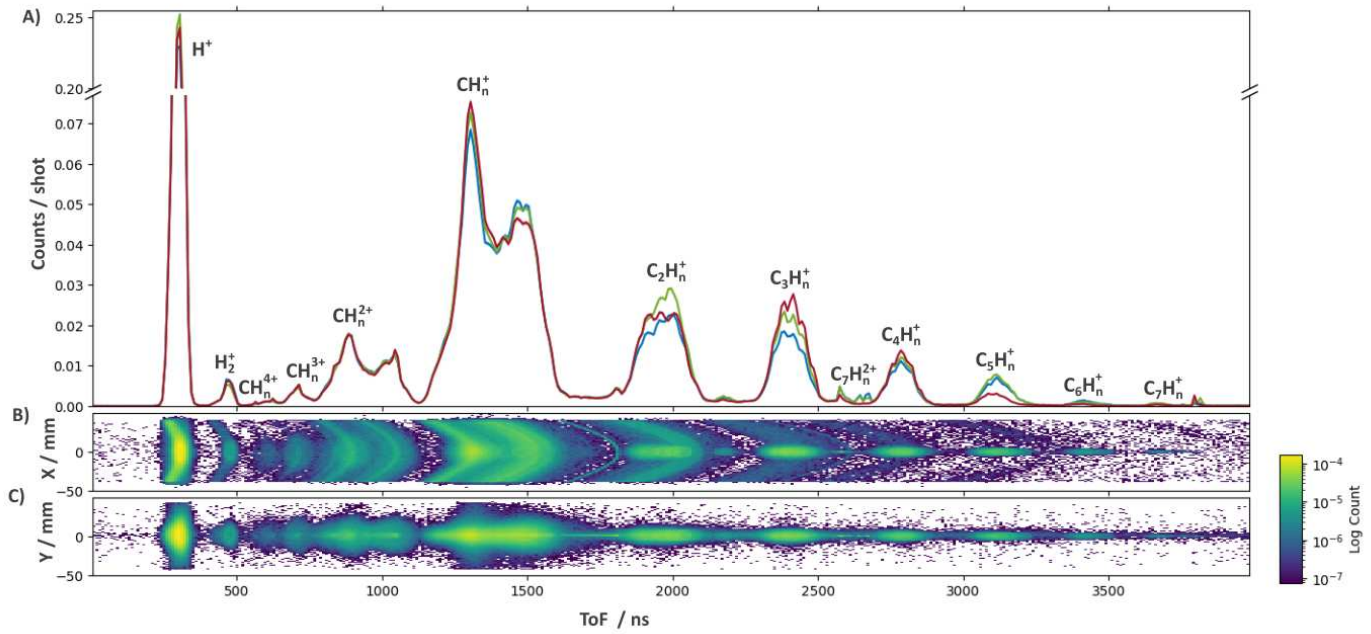


Fig. 1 A) Ion time-of-flight spectrum for the three different isomers after ionization by 1.5-keV XFEL pulses with an average single-shot pulse energy of 4 mJ. The subscript n denotes the fact that each peak consists of several overlapping contributions from fragments containing a different number of hydrogen atoms, including $n=0$. For the CH_n^{2+} and CH_n^+ peaks, the strongest contribution on the left-hand-side of each peak is from C^{2+} and C^+ , respectively. B) and C) Ion yield as a function of time-of-flight and hit position for toluene.

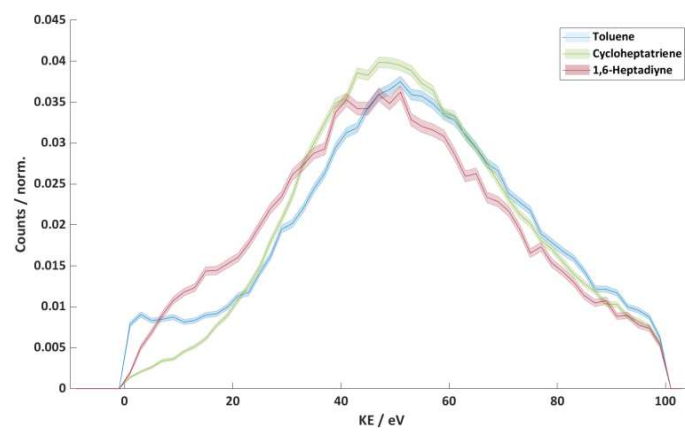


Fig. 2 Experimental kinetic-energy spectrum of the C^{2+} ions when selecting a coincidence of three C^{2+} ions.

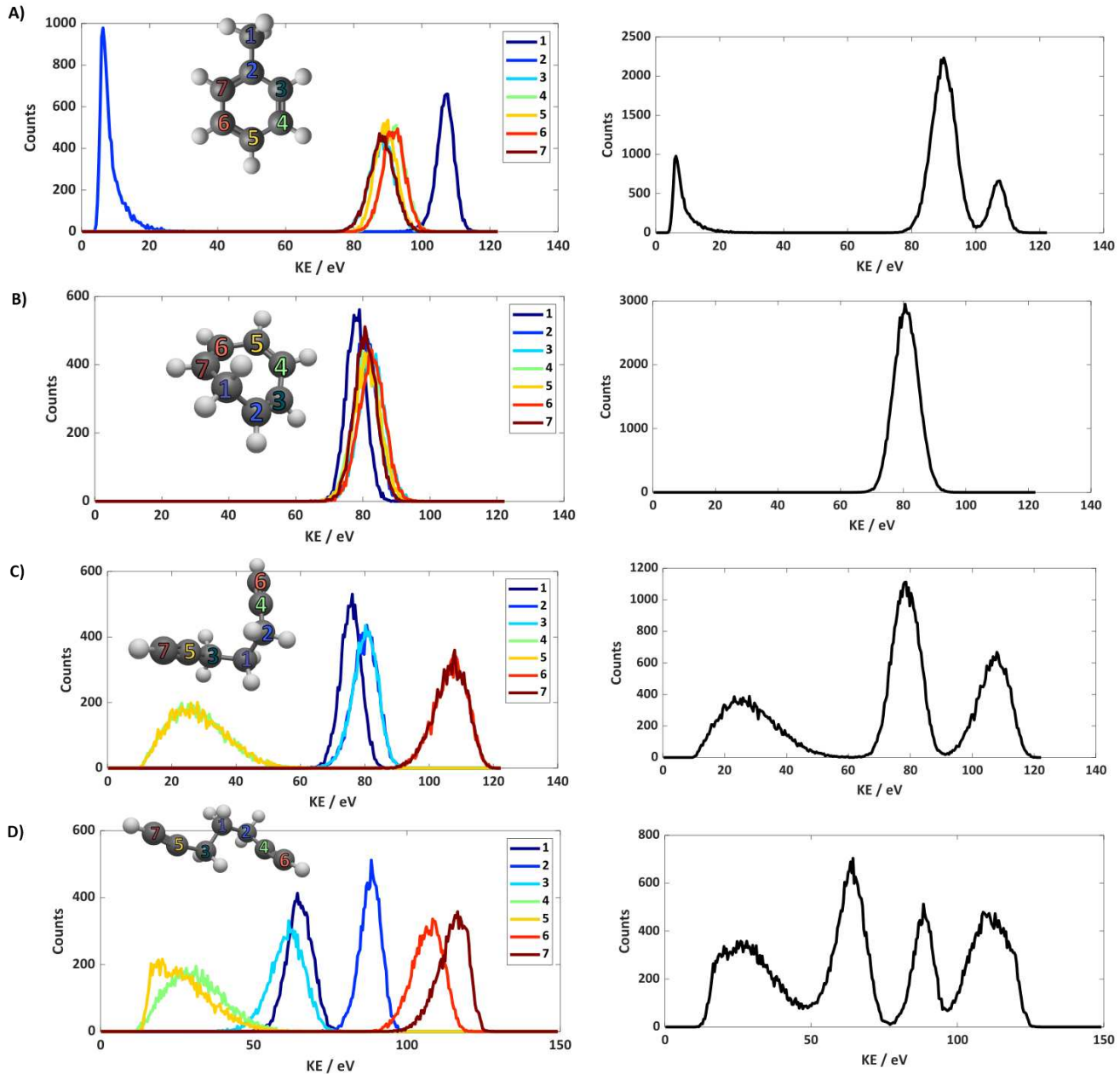


Fig. 3 Simulated kinetic-energy spectra for a charge of 2+ on all carbon fragments for A) toluene, B) cycloheptatriene, C) the GG-trans conformer of 1,6-heptadiyne, and D) the AG conformer of 1,6-heptadiyne. The individual kinetic-energy spectra for each carbon site are color-coded in the left column, while the panels on the right show the total spectrum with the contributions from all carbons added. The corresponding experimental spectra are shown in Supplementary Fig. 2.

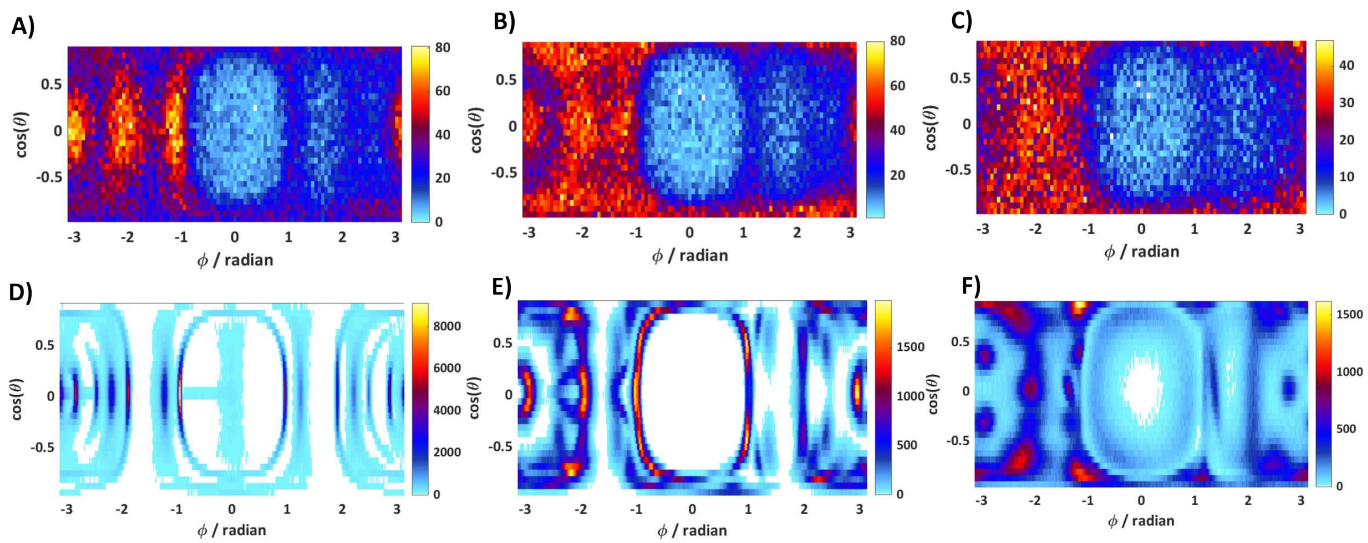


Fig. 4 Experimental (top row) and simulated (bottom row) molecular-frame angular emission distributions in spherical coordinates for C^{2+} ions when combining all reference ions. A) and D) Toluene; B) and E) cycloheptatriene; C) and F) 1,6-heptadiyne (simulation contains only the GG-trans conformer geometry).

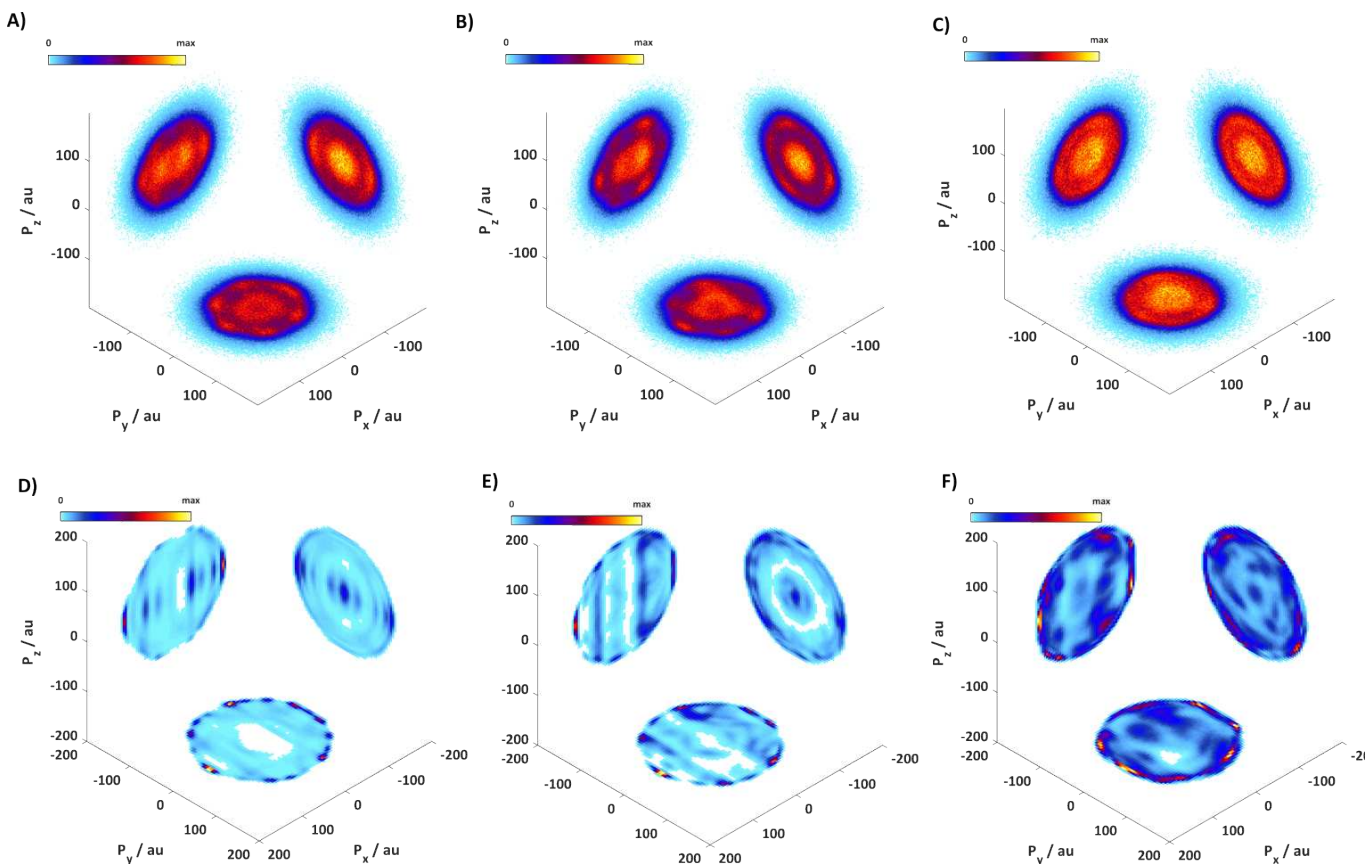
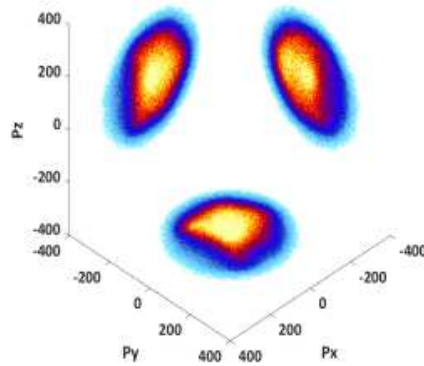
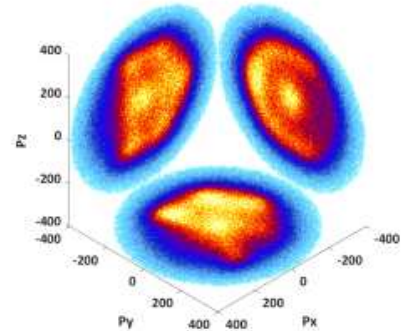


Fig. 5 Experimental (top row) and simulated (bottom row) Newton plots for H^+ ions from the $\text{H}^+ + \text{C}^{2+} + \text{C}^{2+}$ coincidence channel, with the recoil frame defined by the two C^{2+} ions, when combining all reference ions. A) and D) Toluene; B) and E) cycloheptatriene; C) and F) 1,6-heptadiyne (simulation contains only GG-trans conformer geometry).

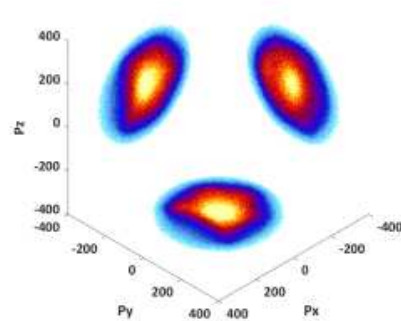
$i=C^+ / j=C^+ / k=C^+$



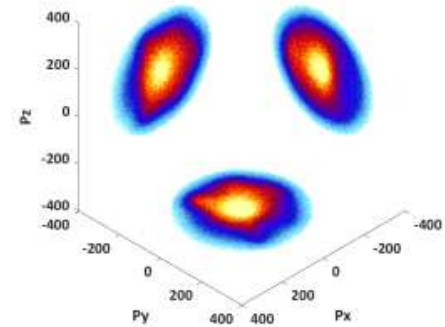
$i=C^+ / j=C^+ / k=C^{2+}$



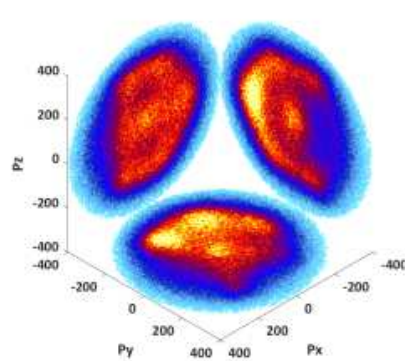
$i=C^+ / j=C^{2+} / k=C^+$



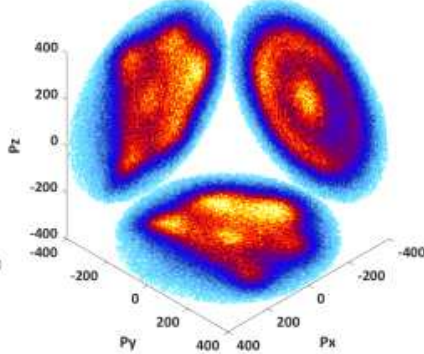
$i=C^{2+} / j=C^+ / k=C^+$



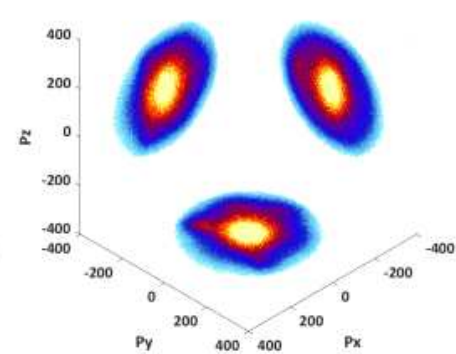
$i=C^+ / j=C^{2+} / k=C^{2+}$



$i=C^{2+} / j=C^+ / k=C^{2+}$



$i=C^{2+} / j=C^{2+} / k=C^{2+}$



$i=C^{2+} / j=C^{2+} / k=C^{2+}$

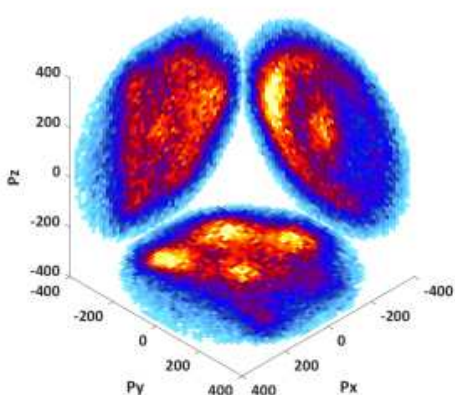


Fig. 6 Experimental Newton plots for toluene from different charge channels and iterations of the recoil frame from the detected ions.

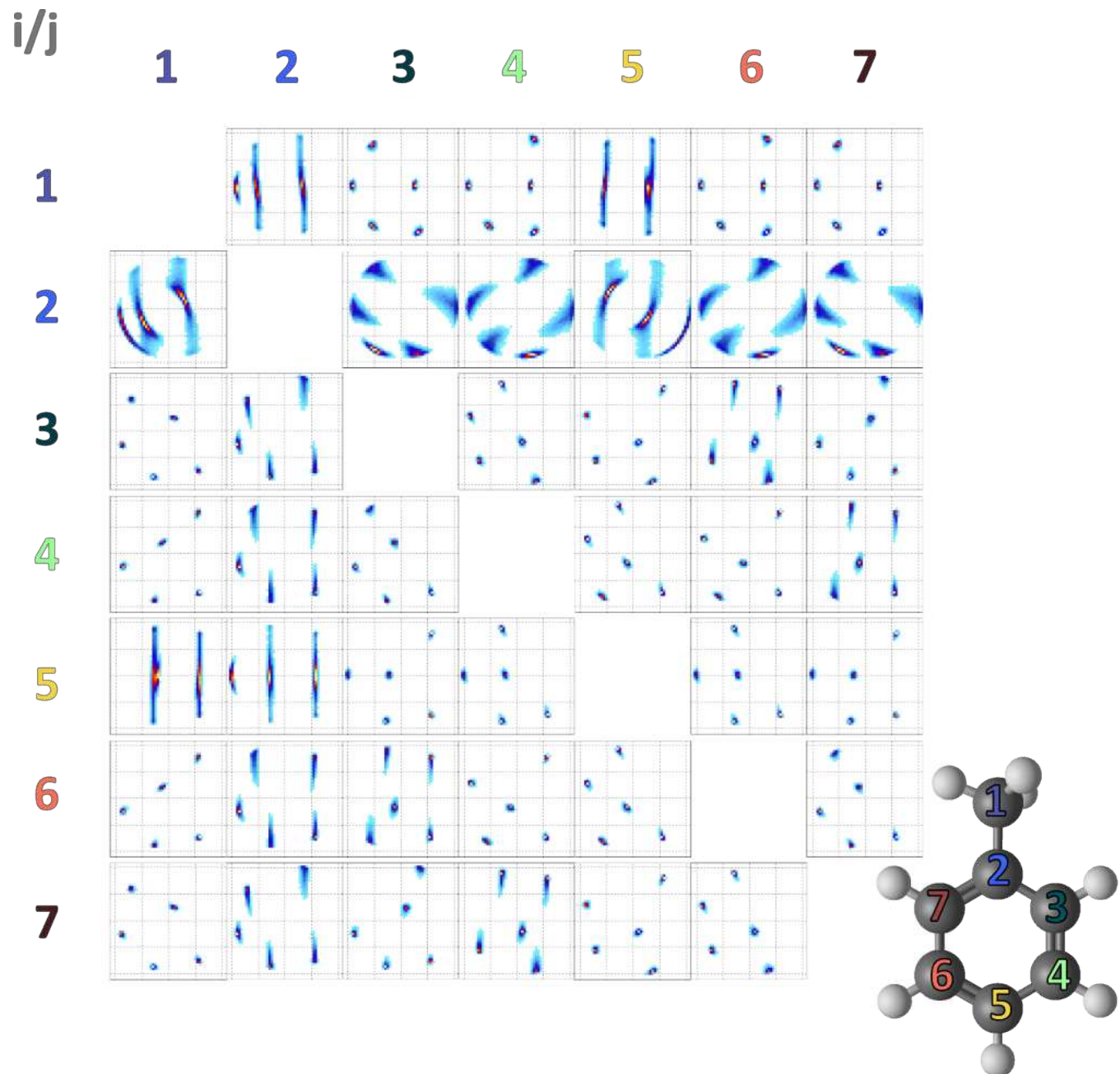


Fig. 7 Simulated Newton plots for toluene iterating through all combinations of reference ions. Each column corresponds to the carbon site whose momenta defines the x-axis. The rows correspond to the carbon site whose momentum vector define the y-axis.

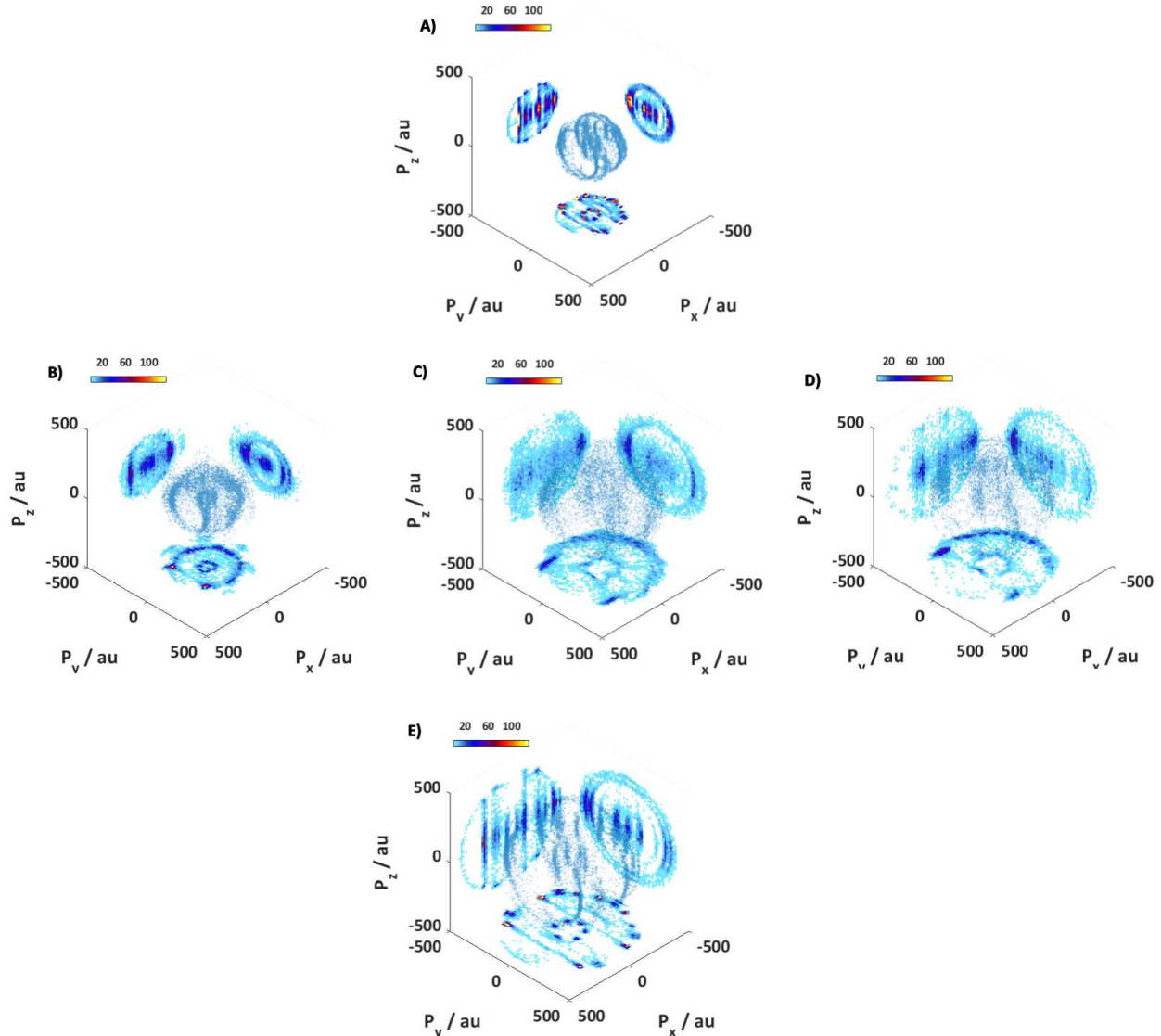


Fig. 8 Simulated Newton plots for toluene from different charge channels and iterations of the recoil frame from the detected ions. A) Example of uniform charge distribution with each carbon having $q = +1$. B) Random charge distribution, where three fragments, each with a charge of $q = +1$, were selected from the ensemble. C) Random charge distribution but with asymmetric selection of the fragments. Two fragments with $q = +1$ were selected, and a third with $q = +2$; the C^+ fragments define the recoil plane, while the C^{2+} ion is plotted. D) Random charge distribution, where three fragments, each with a charge of $q = +2$, were selected from the ensemble. E) Uniform charge distribution with each carbon ion having a charge of $q = +2$.